SAMURAI-S: Sonic Anemometer on a MUlti-Rotor drone for Atmospheric turbulence Investigation in a Sling load configuration

Mauro Ghirardelli[1,3], Stephan T. Kral[1,2], Etienne Cheynet[1], and Joachim Reuder[1,2]

[1]Geophysical Institute and Bergen Offshore Wind Centre, University of Bergen, 5020 Bergen, Norway.
[2]Bjerknes Centre for Climate Research, 5020 Bergen, Norway.
[3]Department of Atmospheric and Cryospheric Sciences, University of Innsbruck, Innrain 52f, Innsbruck, Austria.

Correspondence: Mauro Ghirardelli (mauro.ghirdelli@uib.no)

Abstract. This study introduces the SAMURAI-S, a novel measurement system that incorporates a state-of-the-art sonic anemometer combined with a multi-rotor drone in a sling load configuration, designed to overcome the limitations of traditional mast-based observations in terms of spatial flexibility. This system enables the direct measurement of 3D wind vectors while hovering, providing a significant advantage in manoeuvrability and positional accuracy over fixed mast setups. The capabilities of the system ~~are~~ were quantified through a series of $10\,\text{min}$ to $28\,\text{min}$ flights, conducting close comparisons of turbulence measurements at altitudes of $30\,\text{m}$ and $60\,\text{m}$ against data from a 60-meter tower equipped with research-grade sonic anemometers. The results demonstrate that SAMURAI-S matches the data quality of conventional setups for horizontal wind measurements while slightly overestimating vertical turbulence components. This overestimation increases ~~as the wind speed increases~~ with wind speed.

1 Introduction

Since the 1960s, ~~mast~~ mast- and tower-based sonic anemometry ~~has~~ have been the standard for high-frequency turbulence measurements in atmospheric boundary layer (ABL) research (Foken, 2006; Mauder et al., 2021). With continuous technological development over the years, state-of-the-art sonic anemometers allow for ~~in-situ flux estimations~~ in situ flux estimation (e.g., Foken et al., 2012) and for the spectral characterization (e.g., Midjiyawa et al., 2021) of turbulence. However, ~~recent~~ several studies in ABL meteorology and wind energy, such as Fernando and Weil (2010), Mahrt (2014), or Veers et al. (2019), highlight the limitations of those traditional tower-based measurements, emphasizing the need for more flexible approaches to address a ~~wider~~ broader range of relevant ABL processes.

Some examples illustrating mast-based measurement limitations include the study of the coherence of turbulence (Cheynet et al., 2018), ~~which is a critical~~ a key design parameter for modern wind turbines. For such an investigation, ~~it would be required to erect~~ erecting multiple 300-meter masts close to each other would be required, which is impractical. The same holds for the detailed investigation of wind turbine wakes within a wind farm, as, e.g., explored by Porté-Agel et al. (2020), as variability in wind speed and direction make a proper positioning of masts in such dynamic conditions practically unfeasible. Other research topics that require alternative sensor carriers ~~are~~ include the investigation of the wave boundary layer (Wu and Qiao, 2022),

air-sea-exchange over the ocean (Taylor et al., 2018), and air-ice-sea interactions in polar regions, e.g., over open water areas
25 within the sea ice (Marcq and Weiss, 2012).

Airborne platforms have been used to extend the range of turbulence-related measurements. Fixed-wing uncrewed ~~aerial vehicles (UAV~~aircraft systems (UASs), often employing multi-hole probes (Mansour et al., 2011; Wildmann et al., 2014a, b; Båserud et al., 2016; Witte et al., 2017; Calmer et al., 2018; Alaoui-Sosse et al., 2019; Rautenberg et al., 2019), have demonstrated their capability in turbulence sampling along the flight track across larger areas. ~~The~~ However, the inability to hover
30 or move very slowly ~~is, however, restricting their ability for measurements in situations that require~~ restricts their ability to measure in situations requiring stationary point measurements or localized vertical profiling.

Conversely, tethersonde systems equipped with sonic anemometers can provide quasi-stationary measurements and are effective in vertical profiling (Ogawa and Ohara, 1982; Hobby, 2013; Canut et al., 2016). ~~Those systems require , however, a considerable logistic~~ However, those systems require considerable logistical effort and have clear operational limits ~~with~~
35 ~~respect to~~ regarding wind speed and atmospheric turbulence~~that~~, which strongly affect their controllability. Consequently, tethered systems cannot be easily deployed in remote areas and complex terrain ~~,~~ or safely operated ~~close to~~ near structures and buildings, ~~e.g.,~~ such as in urban areas or ~~the vicinity of~~ near wind turbines and wind farms.

Rotary-blade ~~UAVs~~ uncrewed aerial vehicles (UAVs) offer a more suitable sensor platform for localized and stationary measurements (Abichandani et al., 2020). Recent studies have explored the use of different methods of atmospheric flow
40 measurements, ~~by either using the drone~~using either the UAV's motion and attitude as a proxy for wind estimates (Segales et al., 2020; González-Rocha et al., 2020; Shelekhov et al., 2021; Wetz et al., 2021; Wildmann and Wetz, 2022), or by mounting ~~of~~ miniaturized sonic anemometers (Palomaki et al., 2017; Li et al., 2023) on the ~~drone~~vehicle. Both methods show limitations for turbulence investigations due to the limited sampling frequency and, for most small sonic anemometers, the inability to measure the full 3D flow. First attempts of flying research-grade sonic anemometers (Hofsäß et al., 2019; Thielicke et al.,
45 2021) have shown promising results ~~with respect to~~ concerning the measurement of the mean wind speed, but full turbulence measurement capabilities are still unproven.

One main reason is that the propeller-induced flow (PIF) by the UAV can affect and disturb the on-board flow measurements. Mounting an extension arm ~~,~~to place the wind sensor either to the front (Hofsäß et al., 2019), to the side, or above the drone (Thielicke et al., 2021) is one obvious possibility to minimize the PIF effect. ~~As any mass outside the center~~ Any mass placed
50 outside the centre of gravity of the UAV ~~system~~ will inevitably compromise flight stability and complicate flight control. Thus, it is necessary to thoroughly investigate and characterize the PIF for appropriate sensor placement considerations (Ghirardelli et al., 2023; Jin et al., 2024; Flem et al., 2024). The second option~~to mitigate~~, which mitigates the potential PIF influence on the measurements ~~, without heavy impact on~~ without significantly impacting flight control and stability, is ~~the deployment of~~ to deploy the flow sensor as a sling load under the drone.
55 Based on the latter concept, this study introduces SAMURAI-S as a novel measurement system for airborne atmospheric research using drones. To the authors' knowledge, this represents the first attempt to deploy a research-grade sonic anemometer as a suspended payload under a UAV, in contrast to the conventional approach of mounting such instruments rigidly to the UAV structure at relatively short distances (typically on the order of decimeters to a meter), as in the studies above.

Carrying the turbulence sampling payload $18\,\mathrm{m}$ under a rotary-wing UAV, the sensor is located outside any measurable PIF effect (Flem et al., 2024). The payload consists of a sonic anemometer, an inertial navigation system (INS), a data acquisition unit, and a mounting frame. This design aims to overcome the limitations mentioned above, thus providing state-of-the-art sonic anemometry data with the added benefits of mobility, hover capability, and adaptable positioning. This will enable detailed turbulence analysis in various settings, including observations close to structures and in urban environments where other methods fail.

This research aims to assess the accuracy and reliability of the developed measurement approach. The methodology involves a comparative analysis between traditional mast-mounted 3D sonic anemometers and the one suspended under the drone. Another key aspect of this study is to evaluate the applicability of a dynamic tilt and motion compensation algorithm to account for the inevitable motion of the payload caused by wind drag and the drone's movements. This algorithm utilizes in situ velocity and attitude data linked to the movement and orientation of the anemometer recorded by the INS. It aims to convert sonic anemometer turbulence measurements obtained from a moving platform into a natural wind or streamline coordinate system, as commonly used in ABL research.

The manuscript is organized as follows: Section 2 details the design of the UAV-payload system. Section 3 introduces the algorithm developed to account for the payload motion. This section also outlines the data post-processing techniques employed in the experimental comparison. Section 4 describes the experimental design for system validation, including the measurement site and the setup of the mast instrumentation. Section 5 compares the integral and spectral flow characteristics derived from the mast- and drone-mounted sonic anemometers. Finally, Section 6 summarizes the main findings of the study and concludes that SAMURAI-S provides a novel airborne instrument platform with a large potential for effectively measuring ambient turbulent flow with unprecedented flexibility.

2 The SAMURAI-S system

2.1 Airframe

Several important design criteria guided the selection of an appropriate airframe. Turbulence measurement with a drone-mounted sonic anemometer requires lifting a payload of roughly $4\,\mathrm{kg}$. This weight estimate results from the required components, i.e., a research-grade sonic anemometer, an inertial navigation system (INS), a battery, a data logger, and a mounting frame. A flight time of at least $15\,\mathrm{min}$ to $20\,\mathrm{min}$ is required to collect turbulent flow time series that allow robust turbulence statistics for variances and covariances, as well as spectral analysis (Van der Hoven, 1957; Kaimal and Finnigan, 1994). Finally, to comply with European regulations for drone operations in the open category, we wanted to limit the UAV's maximum take-off weight (MTOW) to $25\,\mathrm{kg}$, which also aids the logistical aspects of deploying the system in the field. At the same time, we considered flight safety, stability, and precision in positioning design priorities since they are crucial in different real-world scenarios, such as operations near infrastructures, human presence, or complex environments.
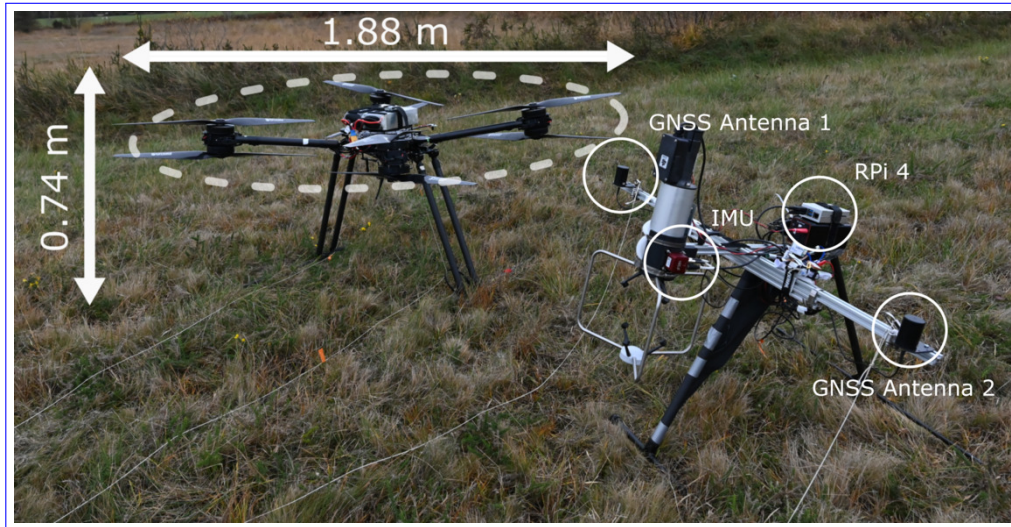
Figure 1. The SAMURAI-S UAS~~including~~, showing the Foxtech D130 octocopter (left) and the sampling payload (right). The D130 is an x8-configuration UAV measuring approximately 1.9m x 0.7m. The payload features a cross-shaped aluminium frame, with a longer arm (0.9 m) supporting two Here3 GNSS antennas and a shorter arm (0.6 m) holding an RM Young 81000 ultrasonic anemometer (mounted upside down) and a Raspberry Pi 4 powered by a dedicated power bank. An IMU is positioned on the side of the anemometer. Key components of the payload are highlighted in the figure.

To address these considerations, we opted for the Foxtech D 130 (Figure 1). This UAV has a nominal maximum payload of $20\,\text{kg}$ and a maximum flight time in hovering mode of up to $45\,\text{min}$ without payload, depending on the atmospheric conditions. It is equipped with eight coaxial contra-rotating propellers, where four pairs of propellers, each driven by brushless electric motors, share the same rotational axis and are mounted on arms extending from the main body (x8 configuration). The configuration of the propellers provides redundancy in case of a motor failure. The ~~UAV's frame~~ frame of the UAV weighs approximately $9\,\text{kg}$. In its default configuration, it is powered by two 6S lithium polymer (LiPo) batteries, each with a capacity of $22\,\text{A}\,\text{h}$, resulting in a take-off weight of roughly $15\,\text{kg}$ excluding the sensor payload. The UAV ~~has an onboard autopilot unit (~~mounts a Cubepilot Cube Orange ~~) combined with 2 GNSS~~autopilot unit combined with two global navigation satellite system (GNSS) antennas (Here3). The inclusion of an open-source autopilot unit in the Foxtech D130's standard configuration, combined with its modular design that supports customization and easy rebuilding, ultimately led us to select this model over other alternatives available on the market.

The UAV's specifications are shown in Table 1.

2.2 Sensor placement

The placement of the sonic anemometer is critical for the quality of the turbulence observations, as it ~~is proven~~ has been shown that placing the sensor at a certain distance from the propellers effectively reduces the impact of the PIF (Prudden et al.,

4

Table 1. Specifications of Foxtech D130

Components	Characteristics
UAV diameter (m) × height (m)	1.88 × 0.74
UAV frame's weight (kg)	9
Propellers	Foxtech Supreme C/F 2880T
Propeller diameter (m) × pitch (m)	0.71 m × 0.20
Propeller's weight (g)	8 × 90
Battery	2 × 6S1P LiPo[*]
Battery's weight (kg)	2 × 2.4
Motors	T-Motor U10II[**]
~~ESC~~ Electronic speed controller (ESC)	T-Motor Flame 80A
Autopilot	Cubepilot Cube Orange[***]
GNNS	Here3 dual antenna
Flight Time (min)	40 to 45

[*] 22 A h; 22.2 V; 30 C

[**] 8.6 kg maximum thrust when paired to Foxtech Supreme C/F Propeller 2880T

[***] ArduCopter v4.3.6 in Aug and v4.4.3 in Dec

2016; Thielicke et al., 2021; Wilson et al., 2022). However, this approach requires ~~an estimation of~~ identifying the volume significantly affected by the PIF, which varies with the UAV's geometry (Guillermo et al., 2018; Lei and Cheng, 2020; Lei et al., 2020). Moreover, the angular momentum resulting from the additional weight mounted outside the UAV's centre of gravity could significantly compromise flight stability.

To limit the influence of the PIF on ~~the~~ velocity measurements, sensors mounted on a boom above the mean rotor plane of UAVs have been used in the past (Palomaki et al., 2017; Shimura et al., 2018; Natalie and Jacob, 2019; Thielicke et al., 2021; Wilson et al., 2022). This mounting configuration is designed to achieve an evenly balanced weight distribution around the drone by aligning the sensor's weight with the UAV's vertical axis and centre of mass. Nevertheless, this point is true primarily in low wind conditions. In scenarios with stronger winds, the drone must tilt further to counteract the increased drag, affecting the initial balance and tilt angle. Finding the right boom length that effectively reduces PIF while maintaining the drone's manoeuvrability and determining its best orientation remains a subject of ongoing research.

Previous studies (Ghirardelli et al., 2023; Jin et al., 2024), based on the Foxtech D130, suggest that the best trade-off between boom length and PIF reduction , while keeping the payload close to the UAV's fuselage , is achieved by positioning the boom upwind, with the sensor at the boom's end. This orientation avoids the areas significantly affected by the PIF as shown by Ghirardelli et al. (2023). However, to fully take advantage of this configuration, it is necessary to automatically align the sensor or UAV with the mean instantaneous wind direction, i.e. requiring an automatic flight control loop such as the "weathervaning"

algorithm recently implemented in ArduCopter v4.4.0 (see https://ardupilot.org/copter/docs/weathervaning.html) or through adjustments in forward flight. To the authors' knowledge, a reliable prototype of this design has yet to be developed.

125   In this study, we ~~adopt~~ present a novel approach, carrying the sonic payload platform as sling load $18\,\mathrm{m}$ under the drone, corresponding to about 26 rotor diameters (D). This setup places the payload in a stable equilibrium state instead of mounting it above the drone. When the payload is suspended beneath the drone, it creates a pendulum, swinging around the point of minimal potential energy. This natural stability allows the payload to stabilize itself through its oscillations, reducing the need for the drone to actively counteract these movements~~actively~~. The PIF features depend more on thrust rather than UAV's

130 geometry in the far field of the drone, i.e., in a distance of more than 5 D from the rotor plane, when the individual rotor downwash regions have merged to one, (Ghirardelli et al., 2023; Flem et al., 2024). This should extend the applicability of the payload set-up to a wider range of multi-copter platforms.

    Simulations and observations were used to estimate the required vertical displacement of the wind sensor below the UAV. As detailed in Ghirardelli et al. (2023), simulations within a domain extending $9.0\,\mathrm{m}$ below the drone ~~,~~revealed that the ambient

135 wind effectively carries away the downdrafts. Notably, airflow closely resembled free-flow conditions at this domain's lower boundary, directly under the drone and ~~in conditions~~ where wind speeds surpassed $2.5\,\mathrm{m\,s^{-1}}$. This observation was further supported by Jin et al. (2024), which utilizes a configuration of three CW Doppler LIDARs to measure the PIF generated by Foxtech D130 in hover. ~~Measurements indicated~~ The measurements indicated a negligible PIF distortion at a distance of $4.5\,\mathrm{m}$ below the Foxtech D130, in an ambient flow of $4.0\,\mathrm{m\,s^{-1}}$. Finally, Flem et al. (2024) showed how, for the same drone model

140 and in the absence of a background flow, the downdraft drops by more than $40\,\%$ in the range between $1.5\,\mathrm{m}$ to $6\,\mathrm{m}$ under the plane of the rotors. An additional empirical confirmation can be derived from visual observations of a multi-rotor drone over the surface of a lake in low wind conditions (Flem et al., 2024), showing that the PIF of the drone does not reach the surface with the UAV hovering at a height of 15 D above the water. To add a margin of safety, we opted to double the distance identified in the CFD simulations.

145 ## 2.3   Payload Description

The payload consists of an RM Young 81000 sonic anemometer, an SBG Elipse-D inertial navigation system (INS) equipped with two GNSS antennas, and a Raspberry Pi 4 (RPi 4) microprocessor serving as a data logger (Figure 1 and Figure 2). The SBG Elipse-D is a compact INS featuring a dual-antenna GNSS receiver. It includes a MEMS-based ~~Inertial Measurement Unit~~ inertial measurement unit (IMU) and uses an ~~Extended Kalman Filter~~ extended Kalman filter (EKF) to fuse inertial and

150 GNSS data. Table 2 and Table 3 provide key specifications of the sonic anemometer and the INS, respectively.

    For the integration of the different sensors, the battery, and the data logger, we constructed a horizontal T-shaped aluminium frame with a $0.55\,\mathrm{m}$ long main bar and a $1.00\,\mathrm{m}$ long crossbar. In addition, we added a T-shaped support leg to better protect the sensors during landing, transport, and storage and a triangular wind vane to aid the sensor alignment with the mean wind direction and dampen lateral and rotational oscillations around the yaw axis.

155   The sonic anemometer was mounted upside down in the front of this frame, with the INS attached via a custom-fitted mounting plate to the side of its cylindrical support structure, assuring parallel alignment of both sensor coordinate systems.
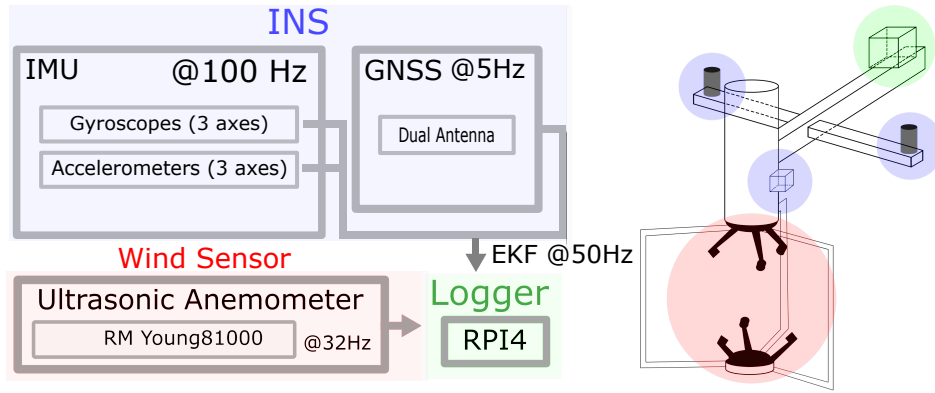
Figure 2. Diagram and blueprint of the measurement and acquisition system showing ~~the~~ how data flow from the sensors ~~to~~ into the logger. On the left, two main sensor outputs –INS (highlighted in blue) and the ultrasonic anemometer (highlighted in red)– are depicted as being stored and logged by the RPi 4 (highlighted in green). The diagram also indicates the sampling rates, namely 32 Hz for the ultrasonic anemometer and a 50 Hz extended Kalman filter (EKF) output from the INS, which fuses data from a 100 Hz IMU signal and 5 Hz GPS data. On the right, a schematic of the payload shows the physical placement of each component, colour-coded to match the diagram on the left.

Table 2. Specifications of RM Young 81000 sonic anemometer.

Specifications	RM Young 81000
Wind Speed Range ($\mathrm{m\,s^{-1}}$)	0 to 40
Wind Speed Resolution ($\mathrm{m\,s^{-1}}$)	0.01
Wind Speed Accuracy ($\mathrm{m\,s^{-1}}$, % RMSE)	±0.05 , ±1,
Wind Dir. Elevation Range ($°$)	±60.0
Wind Dir. Resolution ($°$)	0.1
Wind Dir. Accuracy[*]($°$)	±2
Sonic Temp. Range ($°$C)	-50 to 50
Sonic Temp. Resolution (K)	0.01
Sonic Temp. Accuracy[*](K)	±2
Air Sample Path (m)	0.15
Output Rate (Hz)	4 to 32
Weight (kg)	1.7

[*] $0\,\mathrm{m\,s^{-1}}$ to $30\,\mathrm{m\,s^{-1}}$ range

The crossbar of the frame served as an attachment point for two nylon ropes used to link the payload to the sides of the UAV and a $0.94\,\mathrm{m}$ long baseline for the two GNSS antennas mounted on the tips of the bar. The data logger and a battery were positioned at the tail of the frame.

Table 3. Specifications of the SBG Ellipse-D inertia navigation system with RTK aiding for airborne applications

Specifications	Ellipse-D[*]
Horizontal position accuracy	$0.01\,\mathrm{m}$
Vertical position accuracy	$0.02\,\mathrm{m}$
Horizontal velocity accuracy	$0.03\,\mathrm{m\,s^{-1}}$
Vertical velocity accuracy	$0.03\,\mathrm{m\,s^{-1}}$
Pitch and Roll accuracy	$0.05°$
Heading accuracy	$0.4°$
Weight INS (including GNSS antennas)	$0.3\,\mathrm{kg}$

[*] data were logged using the sbgBasicLogger program (sbgECom library v3.2.4011, https://github.com/SBG-Systems/sbgECom)

160 The attachment points for the ropes were aligned with the pitch axis of both the UAV and the sling load (SL) frame. The entire payload system was balanced for the sonic anemometer's pitch by shifting the position of the crossbar, the battery, and the data logger. According to this payload design and placement, the roll motion is directly transferred to the sonic anemometer from the drone, whereas the yaw motion results from a combination of the drone's dynamics and aerodynamic drag, and the pitch depends mainly on the

165 payload balance. Although the drone-payload setup behaves like a compound pendulum due to the two suspension ropes attached to the same weight (the payload), it has been treated as a simple pendulum for simplicity. The natural oscillation period (T) is estimated using the formula $T = 2\pi\sqrt{\frac{l}{g}}$, where l is the length of the ropes, and $g = 9.81\,\mathrm{m\,s^{-2}}$ is the gravitational acceleration. This calculation yields an oscillation period of approximately $8.5\,\mathrm{s}$, corresponding to a frequency of $0.12\,\mathrm{Hz}$. Preliminary analysis of the sonic data, conducted before performing the motion compensation, consistently revealed a

170 distinct peak at this frequency across all flights.

2.4 Flight Operation

The operation of the SAMURAI-S UAS requires a team of three: a radio control (RC) pilot, a ground control station (GCS) operator, and a payload operator. Before each flight, the UAV and the payload are positioned approximately $10\,\mathrm{m}$ apart. The UAV batteries are securely connected, and a telemetry and an RC link are established. The two ropes are attached to two

175 release servos on the UAV, ensuring that they are free of entanglement with the landing gear or ground obstacles. The payload is powered on and held steady to allow proper IMU initialization and gyro calibration. Finally, the operator connects to the RPi 4 hotspot to verify data streams from the sonic anemometer and the INS, checking for stable GNSS signal and EKF solutions.

During take-off, the payload operator holds the payload steady while the RC pilot executes a vertical ascent to an altitude of approximately 10 m, ensuring that the ropes lift freely without entanglement. Once the ropes are taut, the payload operator releases the payload, and the RC pilot increases the ascent speed. From this point onward, the flight typically continues in auto-mode, following a predefined flight plan, including an algorithm to actively adjust the UAV's heading to face the wind (weathervaning).

Throughout the flight, the GCS operator monitors the system's performance and payload data as long as the WiFi connection to the RPi 4 is maintained. After completing the programmed flight plan, the RC pilot can manually or automatically trigger a return-to-launch (RTL) command. In addition, other fail-safe mechanisms, including low battery, are set to trigger an automatic RTL command based on preset conditions.

During landing, the RC pilot takes control as the UAV approaches the landing area, while the payload operator prepares to catch the payload. During the initial fast descent phase, the UAS is flown diagonally to avoid potential stability issues, such as the vortex ring state (Chenglong et al., 2015; Talaeizadeh et al., 2020). The UAV then descends slowly, with the pilot counteracting any swaying of the payload to ensure a smooth catch. Once the payload is secured, the GCS operator releases the ropes via the servos. The RC pilot then increases the distance between the UAV and the payload before initiating the final landing phase. When the UAV is landed, the payload is placed on the ground, and the data acquisition is stopped. After each flight, the data from the payload and flight controller are downloaded and quickly checked, the UAV and payload are powered off, and the batteries are recharged for future flights.

The system consistently performs excellently, showing no stability issues during the flight, take-off, or landing phases, even under strong wind conditions of up to $15\,\mathrm{m\,s^{-1}}$.

3 Payload data processing workflow

This section outlines the methodological approach to convert the raw flow data sampled by the payload into the natural wind vector expressed in the standard meteorological coordinate system. One primary challenge is ~~the handling of~~ handling asynchronous raw sensor ~~outputs~~ output expressed in different coordinate frames. In addition, it is necessary to compensate ~~the measurements~~ for the motion of the payload. The workflow herein presented addresses both points through a three-stage process~~: first~~. First, the sonic and INS outputs ~~are~~ were filtered to remove faulty data and outliers~~, enhancing their quality and reliability~~. Next, ~~INS and sonic output are~~ these outputs were synchronized, creating a unified temporal framework. Finally, dynamic rotational and translatory transformations ~~are~~ were applied to account for changes in the orientation of the payload and its movements, which primarily come from swinging motions during hovering. For clarity, we first introduce the reference systems~~that~~, which describe the coordinates in which the data are collected and the rotations performed.

3.1 Wind vector, coordinate frames and transformation

We here define two right-handed coordinate systems to describe the motion of the payload: the inertial frame and the body frame, denoted by the indices $\mathbf{i}_n$ and $\mathbf{b}_n$ $(n = 1, 2, 3)$, respectively. The inertial (or NED) frame is Earth-fixed, and its axes
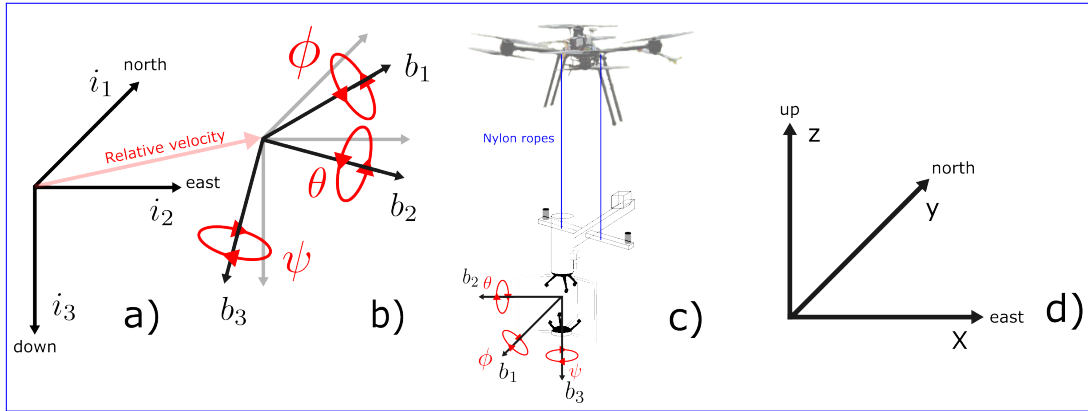
Figure 3. Panel (a) illustrates the inertial frame (NED), where the axes i_1, i_2, and i_3 point northward, eastward, and downward, respectively. Panel (b) depicts the body frame centred at the sonic anemometer's sampling volume, with axes b_1, b_2, and b_3 pointing forward, to the right, and downward. This panel also includes the Euler angles ϕ, θ, and ψ depicting the orientation of the body frame relative to the inertial frame, along with the relative velocity vector $\mathbf{V}_i^b$. Panel (c) illustrates how the payload is attached to the drone by two nylon ropes so that the drone's motion influences the payload's body frame. This configuration causes the payload to inherit the drone's yaw (ψ) and roll (θ) motions while allowing it to pitch freely. Finally, panel (d) shows the meteorological frame ~~used to represent~~ that represents the wind vector $\mathbf{U}$, with ~~axes oriented~~ eastward, northward, and upward axes.

210   (i_1, i_2, i_3) are oriented northward, eastward, and downward, respectively (Figure 3a). The body frame is centred at the sonic anemometer's sampling volume and moves along with the payload. Its axes are defined based on the geometry of the payload, with b_1 pointing forward, b_2 to the right side, and b_3 downward (e.g., Palomaki et al. 2017). Its orientation (attitude) and movements relative to the inertial frame can be described by the Euler angles and the velocity vector measured by the INS, respectively (Figure 3b).

215   To transform the raw flow measurements from body frame coordinates ($\mathbf{V_b}$) to inertial frame coordinates ($\mathbf{V_i}$), a rotation matrix $R(\phi, \theta, \psi)$ is applied (Beard and McLain, 2012; Wetz et al., 2021). This matrix, defined by the roll, pitch, and yaw angles (ϕ, θ, and ψ), adjusts the raw wind vector to reflect the orientation of the payload relative to the inertial frame ~~,~~ and is fully detailed in Appendix A. By subtracting the relative velocity vector $\mathbf{V}_i^b$, accounting for the movement of the body frame relative to the inertial frame, it is ~~in addition~~ possible to eliminate any component of the velocity due to the motion

220   of the payload, isolating the natural wind vector in the inertial frame. The equation that accounts for both of these dynamic corrections is expressed as:

$$\mathbf{V_i} = R(\phi, \theta, \psi)\mathbf{V_b} - \mathbf{V}_i^b. \tag{1}$$

A final orthogonal rotation by right angles is ~~performed~~ needed to retrieve the wind vector (**U**) in the standard meteorological coordinate frame, the natural wind coordinate system, with x, y, and z pointing east, north, and up, respectively (Figure 3c).

$$\mathbf{U} = \begin{pmatrix} 0 & 1 & 0 \\ 1 & 0 & 0 \\ 0 & 0 & -1 \end{pmatrix} \mathbf{V}_i \tag{2}$$

3.2 Data filtering

The sonic anemometer, providing the three wind velocity components and the sonic temperature, was set to a sampling frequency of $32\,\mathrm{Hz}$. Each data instance ~~is~~ was timestamped according to the ~~Raspberry Pi~~ RPi 4 internal clock. Since the ~~Raspberry Pi~~ RPi 4 does not have a GNSS signal, the internal clock does not necessarily correspond to the exact UTC. Therefore, these time stamps ~~are~~ were converted to µs from the start of the logging interval, using the first recorded timestamp as an offset. ~~In addition, the time series were adjusted to account for the upside-down mounting orientation of the sonic anemometer, ensuring that the measured vectors were appropriately rotated in the body frame coordinates before processing.~~

The raw INS output consists of $100\,\mathrm{Hz}$ IMU data and $5\,\mathrm{Hz}$ GNSS data. The IMU provides angular rates (gyroscope data) and accelerations (accelerometer data), while the GNSS supplies the local velocity, latitude, longitude, altitude, and roll and yaw angles. Furthermore, the INS outputs ~~Kalman-filtered (EKF)~~ EKF data at $50\,\mathrm{Hz}$, fusing inputs from both GNSS and IMU. It consists of 3D velocity data and Euler angles, both given in the NED inertial frame, as well as latitude, longitude and altitude data. Given the prototype nature of the developed system, the data processing was exclusively based on the EKF output (Table 3).

Moreover, the SBG Ellipse-D INS allows ~~to output~~ the output of position, velocity and attitude data at a geometrically specified location relative to the sensor. For convenience, we thus configured the INS to output data in the body frame centred on the sonic anemometer measurement volume. Each data point from the INS ~~is~~ was timestamped with the INS internal time in ns from the start of the data log and in UTC post-GNSS signal acquisition. Figure 2 shows a schematic representation of the payload system.

Before any steps in the filtering workflow, the raw time series were adjusted to account for the sonic anemometer's upside-down mounting orientation. This ensured the measured vectors were appropriately rotated in the body frame coordinates.

As an initial filter, we removed all data collected before establishing a valid and stable GNSS time. Following this, data points exceeding the measurement range of the instruments were discarded from further analysis. The filtering thresholds were determined based on the sensor specifications provided by the manufacturers. Additionally, following a despiking method adopted from Mauder et al. (2013), outliers were removed using a moving absolute deviation (MAD) filter relying on a sliding window of $10\,\mathrm{s}$ and a distance of ± 7 MAD from the median. ~~Missing or flagged data accounted for less than 2 % of all the collected data for each individual flight~~ The combined amount of missing and flagged points, following this procedure, did not exceed $2\,\%$ in any flight data set. Thus, they were filled using linear interpolation. The third and final step of the filtering process consisted of identifying the time windows corresponding to the hovering state of the drone. This involved a two-step filtering approach. Initially, a filter was applied based on the median altitude $\pm\,3\,\mathrm{m}$, followed by a $\pm\,4\,\mathrm{m}$ median filter on

11
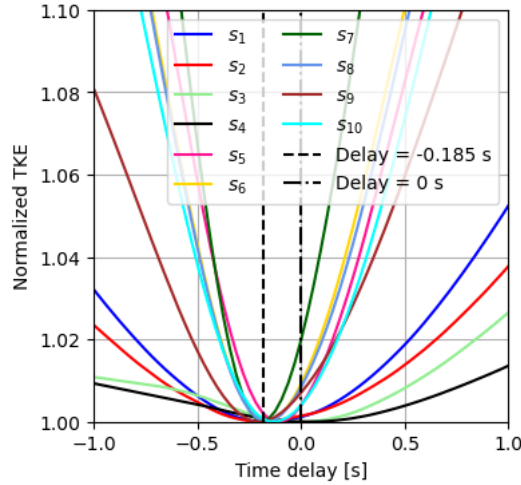
Figure 4. Normalized ~~Turbulent Kinetic Energy~~ turbulent kinetic energy (TKE) curves across validation flights (named s_1 to s_{10}) plotted as a function of time delay (in seconds) of the sonic anemometer output relative to the INS output. Each TKE profile is normalized by its minimum value to facilitate direct comparisons. Vertical lines at $-0.185\,\text{s}$ (dashed line) and $0\,\text{s}$ (dash-dot line) indicate the time window where all minimum values are located. The axes limits are set to -1 to 1 for the x-axis and 1 to 1.1 on the y-axis to highlight subtle differences among the profiles.

255   horizontal movements to address horizontal swinging. Finally, the EKF output ~~is then~~ was downsampled to $32\,\text{Hz}$ to match the sampling frequency of the sonic anemometer via linear interpolation.

3.3   Data synchronization and coordinates transformation

Ensuring accurate synchronization between the INS and the sonic anemometer outputs is crucial for correctly applying Equation (1), designed to compensate for payload motion during flight. To address potential synchronization discrepancies, we

260   implemented an iterative process that involves progressively changing the time lag of the sonic anemometer relative to the INS within a range of $\pm\,2\,\text{s}$, with each step corresponding to $1/32\,\text{s}$. At each adjustment step, Equation (1) ~~is~~ was applied to the sonic data, and we ~~calculate~~ calculated the mean turbulent kinetic energy (TKE) from the resulting time series~~.~~, defined as

$$TKE = \frac{1}{2}\left(\sigma_u^2 + \sigma_v^2 + \sigma_w^2\right). \tag{3}$$

Notably, the TKE as a function of the time lag consistently shows a reverse bell shape with the minimum located between

265    $-0.185\,\text{s}$ to $0\,\text{s}$, as shown in Figure 4. Apart from the location of the time lag, this figure also indicates that potential errors associated with an imperfect time-lag correction, e.g. by a few time increments, would result in small relative errors in the computed TKE.

The time series adjusted using the time lag that minimizes the TKE were selected for further analysis. This selection was based on the assumption that the payload movement is most effectively compensated at this optimal lag. Finally, these time series were transformed into natural wind coordinates using Equation (2).

4 Data and methods for the validation experiment

The validation study was conducted at the Plateforme Pyrénéenne d'Observations Atmosphériques (P2OA) in Lannemezan, southwestern France, during two special observation periods in August and December 2023, as part of the Model and Observation for Surface Atmosphere Interactions (MOSAI) campaign. During these periods, the SAMURAI-S, reusable radiosondes, multiple eddy-covariance stations, meteorological masts, and various remotely piloted aircraft systems were used to study the effects of surface heterogeneities on the local wind conditions. Additionally, a tethered balloon equipped with a sonic anemometer (Canut et al., 2016) provided a complementary method for assessing atmospheric turbulence. While this constitutes an important experimental dataset, the current work focuses solely on validating the SAMURAI-S system. Detailed analysis of the scientific data from the experimental campaign is reserved for future publications.

The P2OA observatory is located in a rural and heterogeneous area, characterized primarily by agricultural fields and forests, with a typical length scale of $500\,\mathrm{m}$ (e.g., BLLAST Lothon et al., 2014). The site has a 60-meter meteorological tower with a triangular lattice structure (Figure 5). The terrain around the tower is predominantly flat and is characterized by a heterogeneous mix of grazing land, grasslands, crop fields, and forest. Within $1\,\mathrm{km}$ of the 60-meter tower, grasslands are more prevalent. The tower is equipped with slow-response sensors for temperature, humidity, wind speed, and direction at five levels ($2\,\mathrm{m}$, $15\,\mathrm{m}$, $30\,\mathrm{m}$, $45\,\mathrm{m}$ and $60\,\mathrm{m}$) and eddy-covariance systems at three levels ($30\,\mathrm{m}$, $45\,\mathrm{m}$ and $60\,\mathrm{m}$), of which only the lower- and uppermost system were operational during our validation period. Two Campbell Scientific CSAT3 sonic anemometers are mounted on horizontal booms on the tower at heights of $30\,\mathrm{m}$ and $60\,\mathrm{m}$ meters above the ground ($633\,\mathrm{m}$ and $663\,\mathrm{m}$ above mean sea level), with an azimuth of $218.0°$ and $230.5°$, respectively. These anemometers operated with a sampling frequency of $10\,\mathrm{Hz}$, recording the three velocity components and the sonic temperature. The validation study described herein comprises several hovering flights of SAMURAI-S at target altitudes of $30\,\mathrm{m}$ and $60\,\mathrm{m}$ near the mast.

4.1 Tower validation study: theoretical framework

For this validation study, we express the wind vector $\mathbf{U}$ in a coordinate system that is aligned with the mean flow streamlines (Kaimal and Finnigan, 1994). In this coordinate system, the three velocity components (u, v, and w) correspond to the along-wind, cross-wind, and vertical (upward) directions, respectively. We apply Reynold decomposition, splitting each component $i = u, v, w$ into a mean, $\bar{i}$, and a fluctuating part, i'. The fluctuating component with a zero mean is treated as a stationary, homogeneous, ergodic, and Gaussian random process. The standard deviations of the u, v, and w components
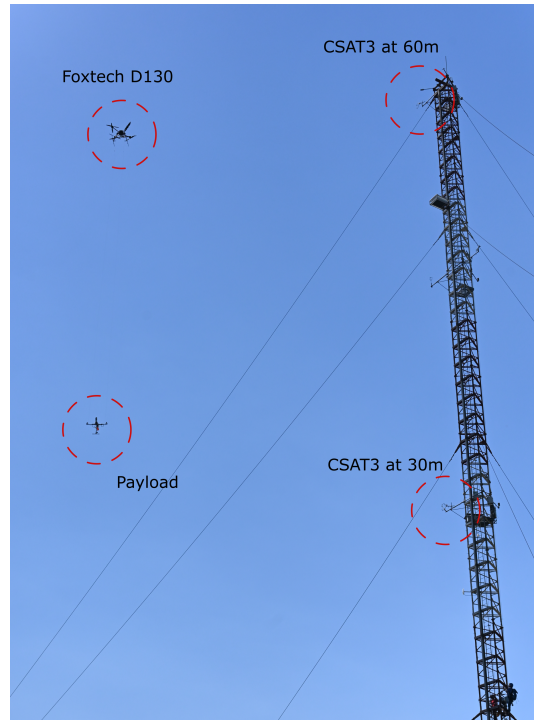
Figure 5. SAMURAI-S hovering side-by-side with the reference mast. The two CSAT sonic anemometers are mounted at $30\,\mathrm{m}$ and $60\,\mathrm{m}$ agl, oriented towards $218.0°$ and $230.5°$, respectively.

are represented by σ_u, σ_v, and σ_w. Additionally, the skewness and kurtosis of these components, which quantify the deviation from the assumption of Gaussian fluctuations, are denoted by γ_i and κ_i.

This study utilizes the blunt and pointed spectral models (Olesen et al., 1984; Tieleman, 1995) to examine whether the velocity spectra conform to the $-5/3$ power law in the inertial subrange. The models are ~~expressed dimensionless as follows:~~ a good approximation of the turbulence spectra in the atmospheric surface layer. In this study, they are expressed in their dimensionless form as

$$\frac{fS_u(f)}{u_*^2} = \frac{a_u f_r}{(1 + b_u f_r)^{5/3}} \tag{4}$$

$$\frac{fS_v(f)}{u_*^2} = \frac{a_v f_r}{(1 + b_v f_r)^{5/3}} \tag{5}$$

$$\frac{fS_w(f)}{u_*^2} = \frac{a_w f_r}{1 + b_w f_r^{5/3}} \tag{6}$$

$$\frac{f\mathrm{Re}\left(S_{uw}(f)\right)}{u_*^2} = \frac{a_{uw} f_r}{(1 + b_{uw} f_r)^{7/3}} \tag{7}$$

14

310 ~~where $f_r = \frac{fz}{\overline{u}}$ represents the reduced frequency, while~~ where a_i and b_i, with $i = \{u, v, w, uw\}$, are coefficients empirically determined ~~.~~ and f_r is a reduced frequency defined as

$$f_r = \frac{fz}{\overline{u}}. \tag{8}$$

The Obukhov length ~~(Foken, 2006)~~ (Monin and Obukhov, 1954) can be calculated as

$$L = -\frac{u_*^3 \overline{\theta}_v}{g\kappa(\overline{w'\theta'_v})} \tag{9}$$

315 where $\overline{\theta}_v$ is the mean virtual potential temperature approximated by the sonic temperature, $\kappa = 0.40$ is the von Kármán constant, and $\overline{w'\theta'_v}$ is the ~~vertical kinematic fluxof virtual potential temperature~~buoyancy flux. The nondimensional stability parameter ζ is defined as $\zeta = z/L$, where z is the height above the surface.

Following Kolmogorov's hypothesis of local isotropy in the inertial subrange, the spectral ratios S_w/S_u and S_v/S_u should converge toward $4/3$ as the frequency increases (Busch and Panofsky, 1968; Kaimal et al., 1972). To compare the effectiveness 320 of the mast-mounted and drone-mounted sonic anemometers in resolving turbulence with minimal flow distortion, we apply a quadrant analysis based on the comparison of the ratio S_w/S_u between the two sensor configurations (Figure 6). In the ideal scenario, data points in this figure would cluster around the centre of the plot, as the $4/3$ ratio is reached by both the drone and mast-based data. Deviations from this ratio could indicate flow distortion caused by the supporting structure, the sensor head, or both (Cheynet et al., 2019; Peña et al., 2019). A spectral ratio approaching but not reaching $4/3$ may suggest that isotropy in 325 the inertial subrange is not achieved within the investigated frequency range (Chamecki and Dias, 2004). A spectral ratio that plateaus without reaching the $4/3$ law may reflect flow distortion, typically manifesting as an underestimation of the vertical velocity component. It should be noted that Kolmogorov's hypothesis of local isotropy in the inertial subrange may not apply under non-stationary conditions, e.g., in very stable atmospheric conditions with intermittent turbulence. Thus, the quadrant analysis was conducted only for samples with a mean wind speed above $2\,\mathrm{m\,s^{-1}}$, which was sufficient in this study to eliminate 330 samples that did not exhibit characteristics consistent with the framework adopted here to describe turbulence.

In this study, the spectral ratios are studied using a limited frequency range of interest, which is computed using the reduced frequency ~~$f_r = fz/\overline{u}$~~f_r (Eq. (8)), and $f_r > 2$ following Kaimal et al. (1972). An upper boundary $f_r < 10$ is also applied to ensure a fairer comparison between the drone and mast data.

4.2 ~~Data processingThe processed data from the payload and those from mast-mounted anemometersare initially~~
335 ~~synchronized using the cross-correlation function between the horizontal~~ Satistical uncertainties

The uncertainties associated with turbulent flux measurements are analysed using the methodology described by Wyngaard (1973); Forrer a[...] . This approach quantifies the random error arising from a fixed averaging period (τ) and the mean wind speed ($\overline{u}$). Within this framework, the uncertainties in the momentum fluxes (a_{uw}, a_{vw}), the buoyancy flux ($a_{w\theta_v}$), and those associated with any
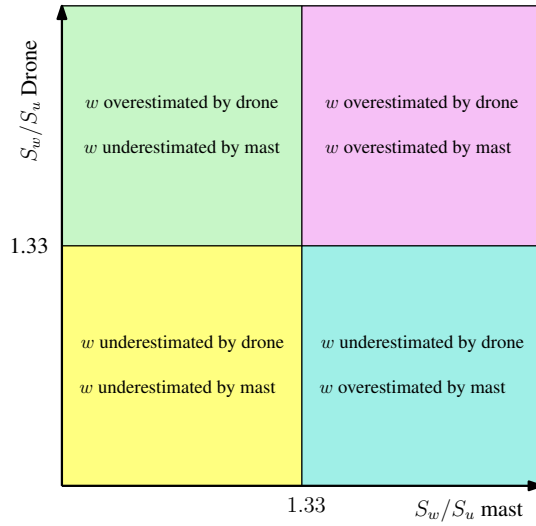
Figure 6. Quadrant analysis of the spectral ratios S_w/S_u to identify which sensor configuration may overestimate or underestimate the vertical velocity component. For brevity, "drone" refers to the drone-mounted sonic anemometer in this figure, and "mast" refers to the mast-mounted sonic anemometer.

turbulent variable ξ are expressed as the following non-dimensional quantities:

$$a_{uw}^2 = \frac{z}{\tau\overline{u}} \left(\frac{\overline{(u'w')^2}}{u_*^4} - 1 \right), \tag{10}$$

$$a_{vw}^2 = \frac{z}{\tau\overline{u}} \left(\frac{\overline{(v'w')^2}}{u_*^4} - 1 \right), \tag{11}$$

$$a_{\theta_v w}^2 = \frac{z}{\tau\overline{u}} \left(\frac{\overline{(w'\theta_v')^2}}{(\overline{w'\theta_v'})^2} - 1 \right), \tag{12}$$

$$a_{\xi^2}^2 = \frac{4z}{\tau\overline{u}} \left(\frac{\overline{\xi'^4}}{(\overline{\xi'^2})^2} - 1 \right). \tag{13}$$

These uncertainties reflect the assumption of ergodicity, which states that the time average converges towards the ensemble average given a sufficiently long averaging period. This assumption is at the core of the turbulence analysis with ultrasonic anemometers. Consequently, these uncertainties are inversely proportional to both the averaging time and the wind speed. Equations (10) to (12) are typically associated with greater uncertainties than Eq. (13), as the estimation of covariance requires a longer averaging period than variance estimates (Kaimal and Finnigan, 1994). The relative magnitude of uncertainties also depends on terrain roughness and stability conditions. Following the recommendations of Stiperski and Rotach (2016); Cheynet et al. (2019), uncertainties below 0.5 indicate high-quality measurements.

4.3 Integral length scales

The integral length scales of turbulence are one-point statistics that quantify the spatial structure of turbulent eddies. These length scales are used both in micrometeorolgy and wind engineering for structural design. One integral length scale can be defined per velocity component. In this study, the integral length scales were estimated in two steps. First, the integral time scale was determined by fitting an exponential function to the autocovariance function of the velocity fluctuations. ~~This aligns the time series of horizontal velocity, correcting any time lags up to 6 s through linear interpolation~~ The autocovariance function for a given velocity component, ξ, is defined as:

$$R_{\xi\xi}(\tau) = \overline{\xi'(t)\xi'(t+\tau)}, \tag{14}$$

where $R_{\xi\xi}(\tau)$ is the autocovariance function at lag τ. The integral time scale, T_ξ, was then obtained by a least-square fit of an exponential function to Eq. (14)

$$R_{\xi\xi}(\tau) \approx R_{\xi\xi}(0) \exp\left(\frac{-\tau}{T_\xi}\right). \tag{15}$$

In the second step, Taylor's frozen turbulence hypothesis was applied to convert the integral time scale into the integral length scale. Taylor's hypothesis is generally valid for moderate and low turbulence intensities. Hereinafter, we define turbulence as "frozen" when the following conditions are satisfied:

$$I_u = \frac{\sigma_u}{\overline{u}} < 0.5 \quad \text{and} \quad \overline{u} > 1 \text{ m s}^{-1}. \tag{16}$$

Under these conditions, the integral length scale, L_ξ, is given by:

$$L_\xi = \overline{u} T_\xi, \tag{17}$$

4.4 Data processing

Data from the payload and the mast-mounted anemometers are collected at different locations. Therefore, the same turbulent structures may be detected at slightly different times due to flow advection. To address this, the two datasets are initially synchronized by an automated procedure that iteratively identifies and applies the optimal time shift (up to a maximum of 6 s) that maximizes the cross-correlation of the horizontal velocity fluctuations. The procedure then uses linear interpolation to align the time series and ensure both datasets capture the same turbulent features. Subsequently, the data are decimated by a factor of 4, and an anti-aliasing finite impulse response (FIR) filter of order 4 is applied. This leads to a sampling frequency of 8 Hz, which was adequate for properly comparing the two datasets.

Misalignments ~~could occur when mounting the sonic anemometer~~ due to small errors in estimating the orientation of the sonic anemometers mounted on the tower or the relative positioning between the INS and the sonic anemometer on the payload can occur. To detect such discrepancies, the datasets from both the payload and the mast (set as the reference) are compared after retrieving the velocity components—namely u, v, and w—using single, double, or triple rotation methods

Table 4. Summary of the ten samples assessed in this study.

Sample ID	Starting Time (UTC)	Duration (~~min~~min)	Mean wind Direction (°°) [*]	Payload height (~~m~~m) [**]	Wind Speed (~~m s⁻¹~~ms⁻¹) [*]	Stability parameter ζ (–) [*]
s_1	21-Aug-2023 14:05:32	28.0	97	28	3.1	-0.46
s_2	07-Dec-2023 12:33:52	18.7	277	27	0.8	0.38
s_3	07-Dec-2023 13:15:26	17.6	265	50	0.4	0.32
s_4	07-Dec-2023 15:08:09	17.8	277	57	0.6	1.25
s_5	08-Dec-2023 15:09:53	10.6	282	56	7.4	0.07
s_6	13-Dec-2023 07:27:17	18.3	300	48	8.2	0.2
s_7	13-Dec-2023 07:53:37	15.3	304	49	10.4	0.1
s_8	13-Dec-2023 08:37:11	15.3	310	23	7.1	0.20
s_9	13-Dec-2023 09:54:21	16.5	298	26	6.5	0.01
s_{10}	13-Dec-2023 10:19:58	20.2	296	49	7.1	0.05

[*] Value estimated by the mast-mounted sonic anemometer closest to the payload height during the hovering window

[**] Average height of the drone during the hovering window.

(McMillen, 1988). While the single rotation aligns u with the mean wind direction, the double-rotation method involves an additional pitch rotation, ensuring $\overline{w} = 0$. In contrast, the triple rotation includes a third rotation around the roll axis to ensure the crosswind component of the kinematic momentum flux $(\overline{v'w'})$ becomes zero. A preliminary comparison involving these three rotations showed limited differences, demonstrating the suitability of the measurement setup. ~~Therefore~~For simplicity, the double-rotation method was chosen for both the mast-mounted and the drone-mounted anemometers for further analysis.

Integral and spectral turbulence characteristics are studied using linearly detrended data. Auto ~~(PSD~~power spectral densities (PSDs) and cross-power spectral densities (~~CPSD~~CPSDs) of the velocity and temperature fluctuations are estimated using Welch's method (Welch, 1967). ~~This involves segmenting~~ We divided the data into three ~~parts~~ segments with 50% overlap. An additional step includes smoothing the PSDs by bin-averaging them over 100 logarithmically-spaced bins (Kaimal and Finnigan, 1994).

5 Results and discussion

In this study, we examine a data set comprising ten samples, labelled s_1 to s_{10} in Table 4, to assess turbulence measurements obtained via the drone-mounted sonic anemometer.

These samples were chosen from 17 initial flights, with the selection criteria based on at least $10\,\mathrm{min}$ of continuous, high-quality EKF output corresponding to hovering flight. Notably, s_2, s_3, and s_4 have mean flows of less than $2\,\mathrm{m\,s^{-1}}$. The assumptions of turbulence being stationary, homogeneous, ergodic, and modelled as a Gaussian random process might not hold for these flights~~. For this reason, they are not subjects of~~, making them unsuitable for the quadrant analysis ~~, the framework~~
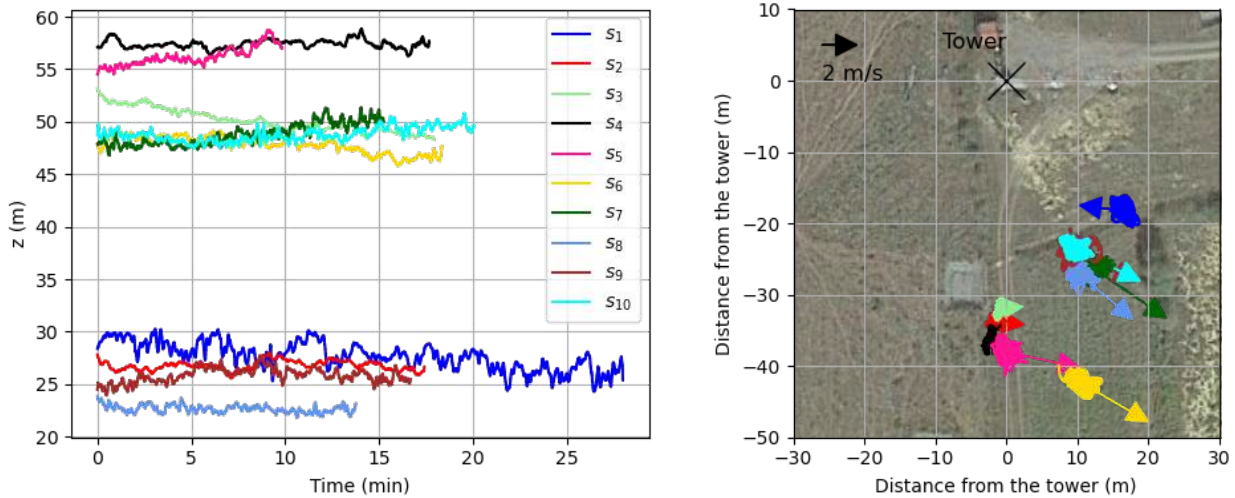
Figure 7. Drone altitude (left panel) and horizontal position relative to the tower (right panel) during the measurement periods of the ten validation flights. The sonic anemometers on the mast are mounted at heights of $30\,\mathrm{m}$ and $60\,\mathrm{m}$, oriented at $218°$ and $230.5°$, respectively. Wind directions for each flight are shown as coloured arrows, originating from the average horizontal positions. The arrow lengths correspond to a reference vector of $2\,\mathrm{m\,s^{-1}}$. Imagery ©2024 Maxar Technologies, Map data ©2024 Google

~~of which is presented~~ framework proposed in Section 4.1. Nevertheless, they ~~are~~ were included in the ~~rest of the analysis for completeness.~~ analysis for the sake of completeness.

Figure 7 shows the associated altitude of the payload above the ground (left panel) and the hovering distance from the tower during the measurement periods (right panel).

Although all flights were analyzed, for brevity, Section 5.1 features a detailed comparison of the exemplary cases from sample s_1 and s_7 as they exhibit markedly different characteristics. Sample s_1 targeted a height of $30\,\mathrm{m}$ and features convective conditions ($\zeta = -0.46$) with rather weak wind of $3.1\,\mathrm{m\,s^{-1}}$. Conversely, sample s_7, which targeted $60\,\mathrm{m}$, is characterized by stable stratification conditions ($\zeta = 0.1$) and the highest wind speed in the series ($10.4\,\mathrm{m\,s^{-1}}$). It will be shown that while s_1 exhibits an excellent correlation between the drone-mounted anemometer and its mast-mounted counterpart, s_7 presents some discrepancies in the vertical component when comparing the two anemometers. Following these detailed examinations, we systematically compare all samples ~~based on their integral flow characteristics~~ in Section 5.2. Finally, we conclude the comparison by presenting flux uncertainties between the drone and mast-based datasets in Section 5.3

5.1 Cases of samples s_1 and s_7

This section focuses first on the second-order structure of turbulence (i.e., variances and covariances) of s_1 and s_7, ~~though the~~ as these samples show strongly contrasting characteristics, as pointed out in the previous section. The third and fourth statistical moments (i.e., skewness and kurtosis) are also briefly discussed for completeness. ~~Results related to temperature are presented~~
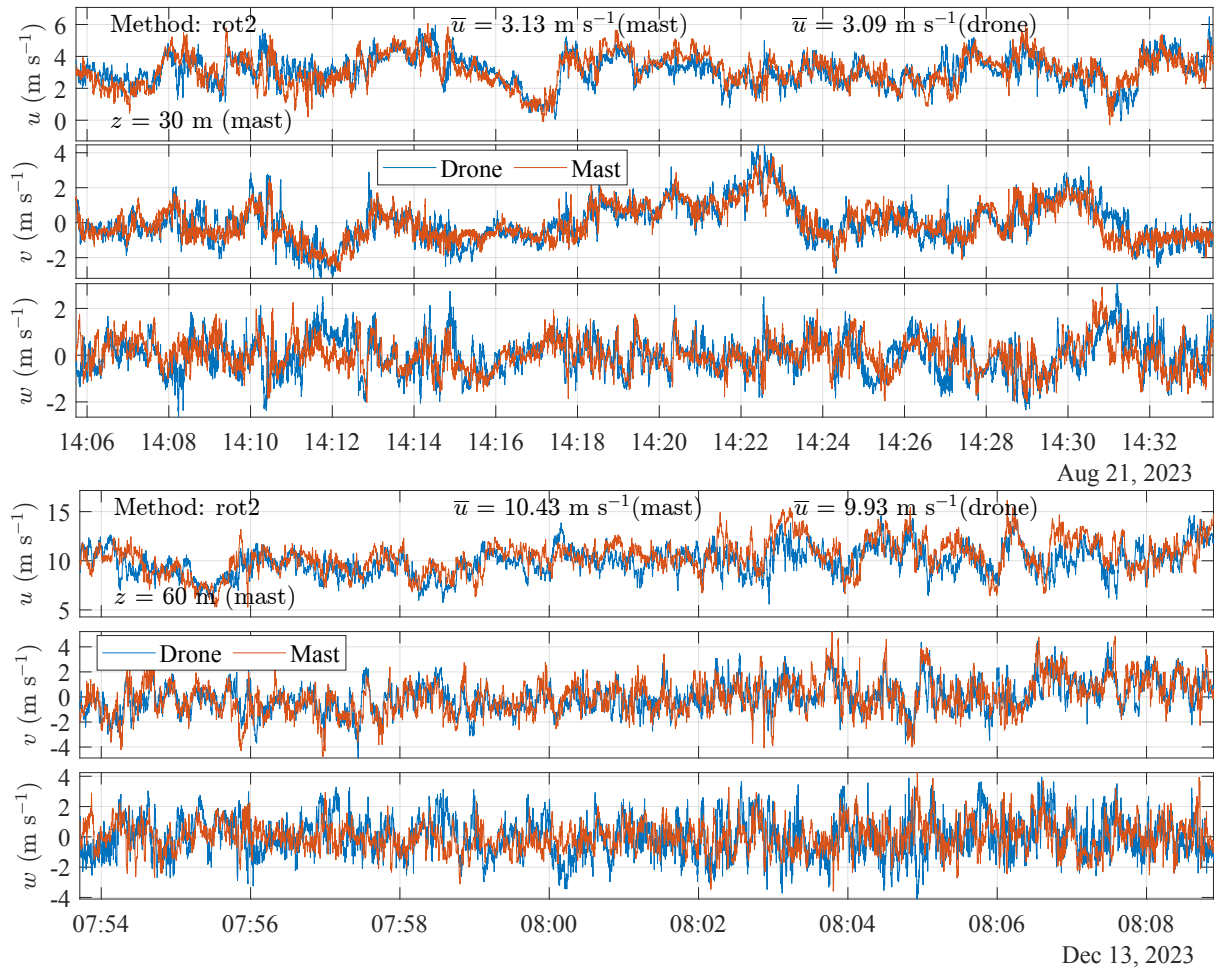
Figure 8. Velocity time series ~~from~~ of the wind components: streamwise (u), crosswind (v), and vertical (w), from drone and mast-based set-ups during flights s_1 (upper panel) and s_7 (lower panel)~~where the SAMURAI-S anemometer is located near~~. The time series from the ~~sonic~~ drone and tower-based setup are coloured blue and orange, respectively. The double rotation (~~samples s_1~~Method: rot2) was applied to both the drone and tower data. The variable z corresponds to the height of the sonic ~~(sample s_7)~~anemometer mounted on the tower, which was the one closest to the drone-mounted sonic anemometer hovering altitude. At the same time, $\overline{u}$ denotes the average streamwise wind component calculated over the sampling period.

~~separately later in the section.~~ Figure 8 presents time series of the velocity components u, v, and w for samples s_1 and s_7. Results related to temperature are presented separately later in the section.

415   Table 5 expands ~~further~~ on this comparison by showing the statistical moments for the three velocity components between the reference mast data and the SAMURAI-S data.

~~The data exhibit a clear similarity, with no noticeable deviations~~ Flow statistics from the drone and mast-mounted sensors are in good agreement, except for the vertical velocity component w of sample s_7, where the drone-mounted sonic anemometer

Table 5. ~~Statistical moments~~ Mean and turbulent flow statistics for samples s_1 and s_7 for drone and mast ~~Data~~data. Samples s_1 and s_7 refer to the samples described in Table 4. σ_i, γ_i, and κ_i, where $i = u, v, w$, refer to the standard deviation, skewness, and kurtosis estimates, respectively. The table also includes the momentum flux values ($\overline{u'w'}$) and buoyancy flux ($\overline{w'\theta_v'}$, respectively) values.

	Sample s_1		Sample s_7	
Statistic	**Drone Data**	**Mast Data**	**Drone Data**	**Mast Data**
$\overline{u}$ ($\mathrm{m\,s^{-1}}$)	3.1	3.1	9.9	10.4
σ_u ($\mathrm{m\,s^{-1}}$)	0.9	1.0	1.4	1.5
σ_v ($\mathrm{m\,s^{-1}}$)	1.1	1.0	1.2	1.3
σ_w ($\mathrm{m\,s^{-1}}$)	0.8	0.7	1.3	1.0
γ_u	-0.2	-0.2	0.0	-0.1
γ_v	0.4	0.4	0.1	0.0
γ_w	0.0	0.3	0.2	0.3
κ_u	3.0	2.7	2.8	3.0
κ_v	3.4	2.8	3.2	3.3
κ_w	2.8	3.4	2.8	3.4
$\overline{u'w'}$ ($\mathrm{m^2\,s^{-2}}$)	-0.2	-0.1	-0.7	-0.5
$\overline{w'\theta_v'}$ ($\mathrm{K\,m\,s^{-1}}$)	0.1	0.1	-0.1	0.0

shows slightly larger fluctuations ($\sigma_w = 1.3\,\mathrm{m\,s^{-1}}$) than those from the mast-mounted sensor ($\sigma_w = 1\,\mathrm{m\,s^{-1}}$). All three velocity components in the mast and the payload data exhibit skewness and kurtosis values close to zero and three, respectively. These measurements indicate Gaussian fluctuations, typically observed ~~in~~ under stationary conditions within the ABL. Despite a $11\,\mathrm{m}$ altitude discrepancy between the sensors (see Figure 7), the drone-mounted sensor accurately tracks short-term horizontal velocity fluctuations. The altitude difference is primarily due to the UAV's altitude control being based on pressure rather than GNSS. Unfortunately, this discrepancy was only noticed during the post-processing phase and was not corrected in the field.

Figure 9 presents the auto power spectral density (PSD) for each velocity component and the real part of the cross-spectrum between u and w for samples s_1 and s_7, plotted on a log-log scale and multiplied by the frequency f to highlight spectral features. The smooth PSD is computed using ~~Equations (4) to (7)~~ Eqs. (4) to (7) that is fitted to the data recorded by the payload sensor. This least-square fit is useful to assess whether the estimated PSD follows the $-5/3$ power law associated with the inertial subrange for the S_u, S_v, and S_w spectra, and the $-7/3$ power law for the co-spectrum $\mathrm{Re}(S_{uw})$. A slightly steeper roll-off is observed for the mast data.

Both sensors consistently capture the along-wind (u) and across-wind (v) velocity components for the selected samples s_1 and s_7. In sample s_1, the S_v spectrum reveals a small peak at approximately $0.20\,\mathrm{Hz}$. This peak cannot be attributed to the oscillation frequencies of the payload, which are established around $0.11\,\mathrm{Hz}$. Thus, it is more likely related to ~~a real flow feature~~ random fluctuations. The co-spectrum between u and w for sample s_1 features unusual positive values in the mast-
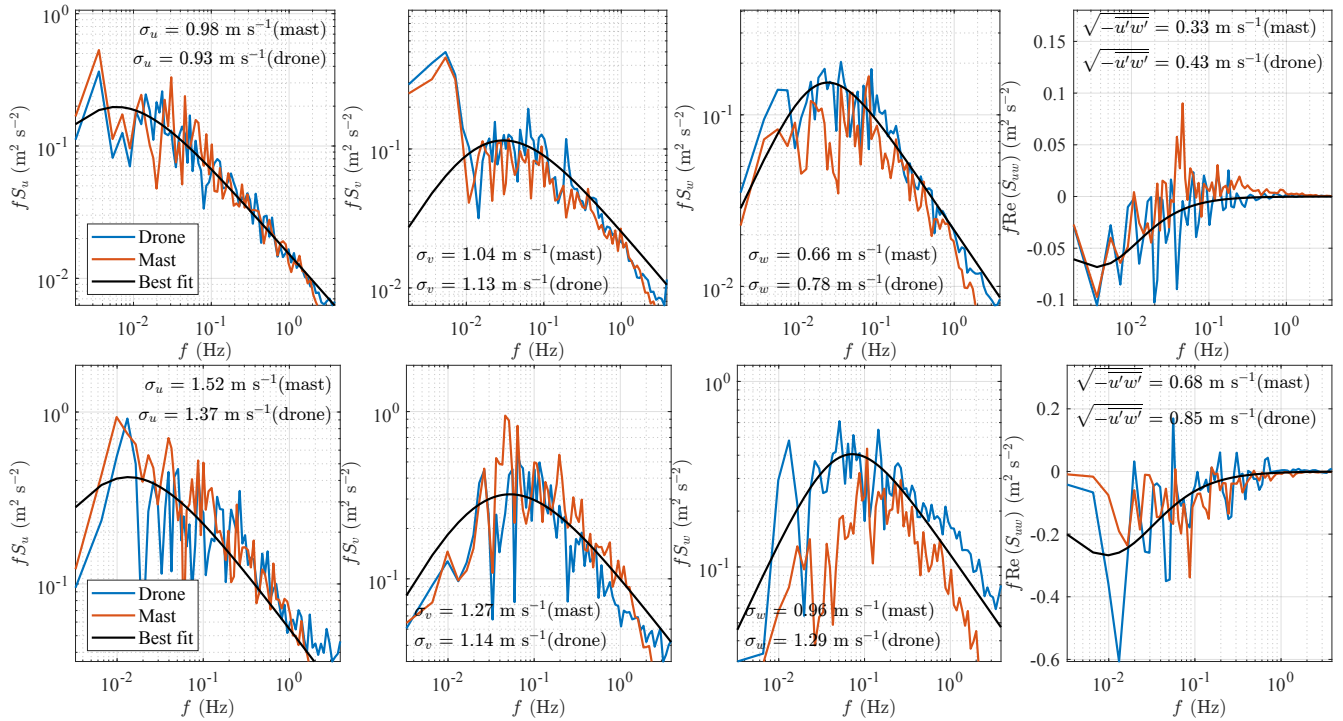
Figure 9. Power spectral density (PSD) estimates of the velocity components ~~for both the flying sonic anemometer~~: streamwise (u), crosswind (v), and vertical (w), as well as the ~~one mounted on the mast at a height of 30 m above the ground for samples~~ co-spectrum ($Re(S_uw)$), from drone and mast-based set-ups during flight s_1 (~~top~~upper panels) and ~~the one mounted at 60 m for~~ s_7 (~~bottom~~lower panels). The solid black line refers to the blunt model (for S_u, S_v, and ~~S_{uw}~~$Re(S_{uw})$) or pointed model (for S_w) fitted to the data from the drone-mounted anemometer. The variances of the velocity components (σ_u, σ_v and σ_w) and the Reynold stress element $\overline{u'w'}$ are indicated within each corresponding plot.

435   mounted data between $0.03\,\text{Hz}$ to $1\,\text{Hz}$, with a distinctive positive peak at $0.04\,\text{Hz}$. These features are not present in the SAMURAI-S data, indicating differences in the flow between those captured by the tower-mounted instrument. This peak is unlikely related to a shadow effect of the tower, given that the wind direction was $97°$ and the tower-mounted sonic sensor is oriented towards $218°$ for s_1.

     For flight s_7, the power spectral density of the vertical component clearly shows a higher energy content at all frequencies

440   recorded by the drone-based sonic anemometer compared to those from the tower (Figure 9). This is consistent with the higher σ_w values from the drone data shown in Table 5. This feature is present in nearly all flights (see Section 5.2), although it is particularly pronounced in s_7.

     The comparative analysis of the sonic temperature time series reveals a good agreement across sample s_1 and s_7, with minor deviations for the mean temperature likely attributable to different calibration values between the sonic anemometers

445   (Figure 10). Further insights are provided by Figure 11, which displays the PSD estimates of the sonic temperature and the
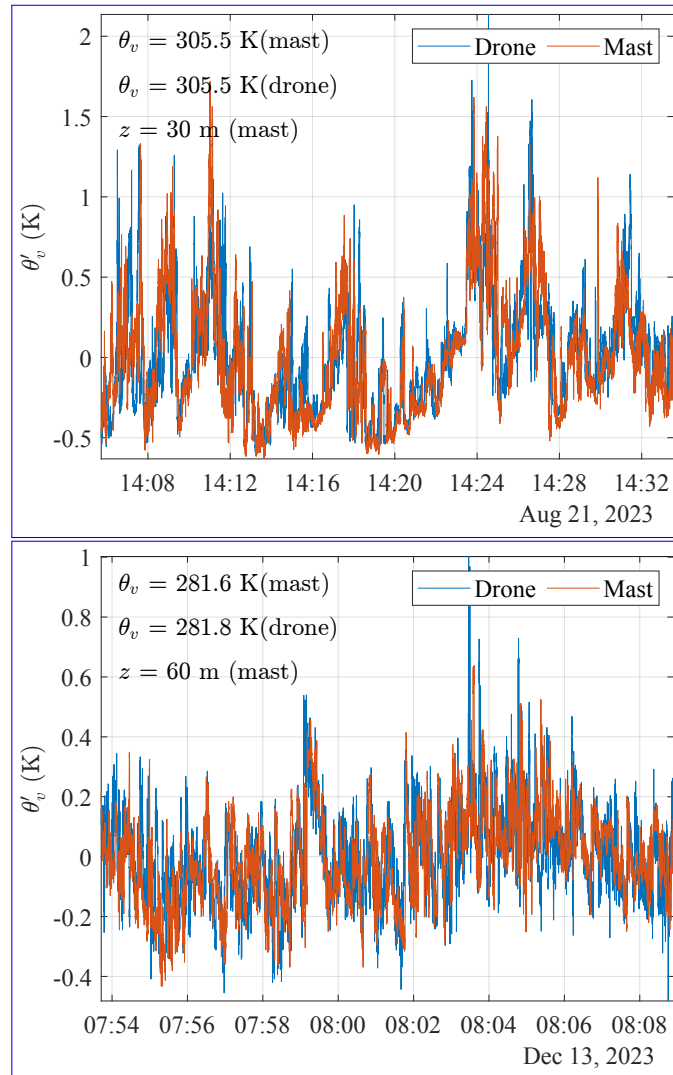
Figure 10. Time series of the fluctuations of the sonic temperature (θ'_w) for samples s_1 (left panel) and s_7 (right panel) measured by the drone-mounted anemometer (blue line) and the mast-mounted sonic (orange line) at a height of $30\,\text{m}$ and $60\,\text{m}$ above the ground, respectively. The mean sonic temperature (θ_v) is also indicated in each panel for both the drone and the mast measurements.

CPSD between the vertical and the along wind component with the virtual potential temperature. Notably, the PSD for sample s_1 demonstrates an excellent agreement between the sonic temperature from the mast-mounted sensor and SAMURAI-S. However, for sample s_7, the PSD of the drone-based anemometer deviates from the expected $-5/3$ power law at frequencies greater than 1 Hz. This deviation scales with frequency f, suggesting the influence of white noise on the measurement data. For the mast-mounted anemometer, the PSD estimates of the temperature exhibit slight discrepancies from this $-5/3$ power
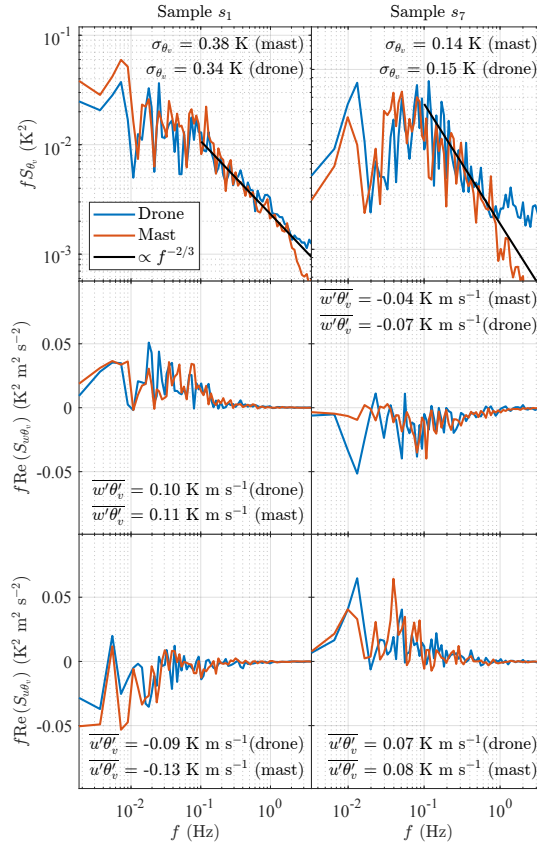
Figure 11. PSD estimates of the sonic temperature ~~fluctuations~~ (θ_v) and associated ~~CPSD with~~ CPSDs, including the vertical $(Re(S_{w\theta_v}))$ and ~~the along-wind~~ along-wind $(Re(S_{u\theta_v}))$ component for both the flying sonic anemometer (blue line) and the one mounted on the mast (orange line) $30\,\mathrm{m}$ above the ground for samples s_1 (left panels) and at $60\,\mathrm{m}$ above ground for samples s_7 (right panels).

law in samples s_1 and s_7. Additional plots showing PSD spectra for samples s_5, s_6, s_8, s_9 and s_{10} are provided in Appendix B.

5.2 ~~Comprehensive~~ Mean and turbulence statistics comparison

~~A comprehensive~~ This section presents a detailed analysis of the sensor performance~~is conducted in this section~~, focusing on
455 integral mean flow and turbulence characteristics for all three velocity components u, v, and w (Figure 12 ~~) for all ten samples.~~
~~Figure 13 compares the covariance-based kinematic momentum, heat fluxes, and stability estimated from the SAMURAI-S~~
~~and the mast-mounted anemometer.~~
and Figure 13). The drone-mounted anemometer slightly underestimates the mean wind speed $\overline{u}$ (Figure 12a), but the data
scatter is low. ~~This underestimation is possibly due to differences in height , since, as it is shown in Table 4~~The height difference
460 between the two sensors may explain this underestimation (Table 4). More specifically, the payload height was on average $4\,\mathrm{m}$
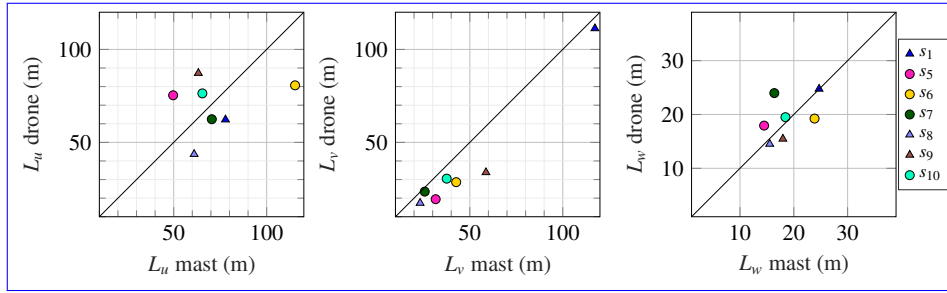
24
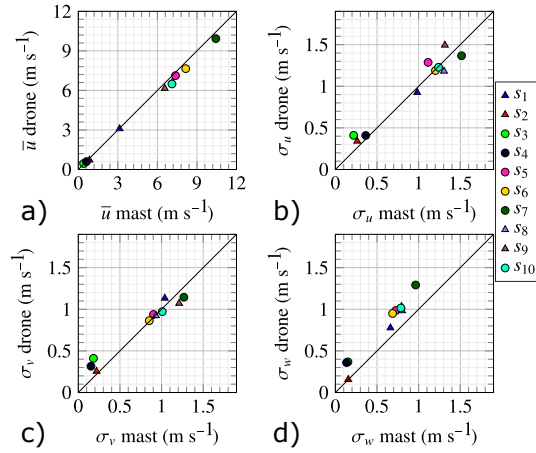
Figure 12. Mean wind speed and standard deviation of the three velocity components for the mast- and the drone-mounted sonic ~~anemometer~~ anemometers across the ten validation samples. Circle markers indicate measurements from the mast at $30\,\mathrm{m}$ above the surface, while triangle markers correspond to measurements at $60\,\mathrm{m}$.
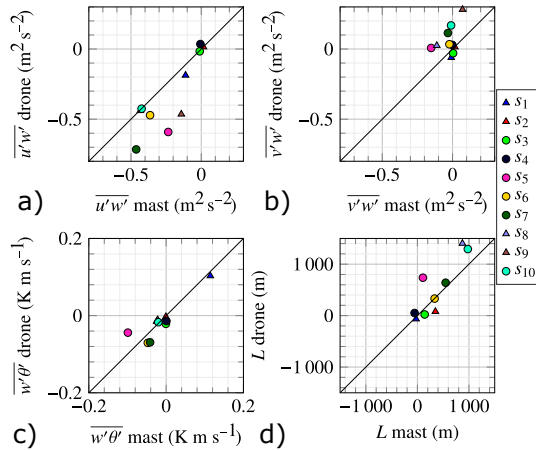
Figure 13. Turbulence covariance and Obukhov length for the ten validation samples, as measured by the mast- and the drone-mounted sonic ~~anemometer~~ anemometers. Circle markers represent measurements from the mast at $30\,\mathrm{m}$ above the surface, whereas triangle markers signify measurements at $60\,\mathrm{m}$.

lower than the target altitude for the sonic at $30\,\mathrm{m}$ and $8.5\,\mathrm{m}$ for the sonic at $60\,\mathrm{m}$. The standard deviations of the along-wind and across-wind velocity components denoted σ_u (Figure 12b) and σ_v (Figure 12c), respectively, show excellent agreement. The drone-mounted anemometer slightly overestimates the standard deviation σ_w of the vertical component (Figure 12d), and this overestimation increases nearly linearly with the mean wind speed in absolute terms.

465   The covariance estimates $\overline{u'w'}$ (Figure 13a) exhibit a larger scatter than $\overline{v'w'}$ (Figure 13b). ~~The covariance between sonic temperature θ' and the fluctuating vertical component w'~~ At the same time, the covariance estimate of $\overline{\theta'w'}$ (Figure 13c), and

25

Figure 14. Integral turbulence length scale of the three velocity components for the mast- and the drone-mounted sonic anemometers across the ten validation samples. Circle markers indicate measurements from the mast at $30\,\mathrm{m}$ above the surface, while triangle markers correspond to measurements at $60\,\mathrm{m}$. Only samples associated with $I_u < 0.5$ and $\overline{u} > 1\,\mathrm{m\,s^{-1}}$ are used to satisfy the conditions required for applying Taylor's hypothesis of frozen turbulence.

the Obukhov length L (Figure 13d) demonstrate good correlation and small scatter. The vertical velocity component is used in the numerator and denominator when calculating L. Thus, the lower scatter may be attributed to the larger uncertainties associated with component w cancelling each other to some degree. Sample s_5, depicted in pink, consistently exhibits the

470 highest scatter. This sample has the shortest duration, lasting only $10\,\mathrm{min}$, which is at least $4.7\,\mathrm{min}$ shorter than all other samples. Thus, sample s_5 may be more prone to errors associated with insufficient sampling of the largest turbulent eddies.

Figure 14 compares the integral length scales for each velocity component, estimated following the procedure presented in Section 4.3. Samples s_2, s_3, and s_4 did not satisfy the conditions required to apply Taylor's hypothesis of frozen turbulence, which were defined as a turbulence intensity of $I_u = \sigma_u/\overline{u} < 0.5$ and a mean wind speed of $\overline{u} > 1\,\mathrm{m\,s^{-1}}$. All other samples

475 met these conditions, with I_u ranging from 0.15 to 0.31 and a mean wind speed exceeding $3\,\mathrm{m\,s^{-1}}$.

The streamwise length scale L_u (Fig. 14, left panel) shows a rather large scatter around the 1:1 line. However, there is no systematic deviation between mast and drone measurements. In contrast, the middle panel suggests that the drone-mounted anemometer systematically underestimates the lateral length scale L_v. However, it is unclear whether this discrepancy arises from sensor characteristics or the specific position of the drone. The best agreement is observed in the right panel for the

480 vertical length scale L_w, which exhibits low scatter and no clear bias, despite the overestimation of σ_w by the drone-mounted sonic anemometer (Fig. 12d).

The discrepancies between the vertical velocity spectral densities estimated by the mast-mounted sonic anemometers and by the drone are explored in more detail through the ratios S_w/S_u and S_v/S_u, following the method presented in Section 4.1. Chamecki and Dias (2004) states that if the spectral ratio trends towards 4/3 without actually reaching it, this could indicate

485 that isotropy in the inertial subrange has not been achieved within the examined frequency range, a situation typically occurring ~~in stable stratification flow~~ under stable atmospheric conditions. In this study, the spectral ratios reached a plateau for all ten samples, albeit not always with a value of 4/3. This suggests that the atmospheric conditions were ~~favorable to the observation of local isotropy ,~~ favourable to observing local isotropy but that flow distortion may have been present. The results for all the samples are shown in Figure 15. Values corresponding to s_2, s_3, and s_4 are displayed with grey triangle markers to highlight

26
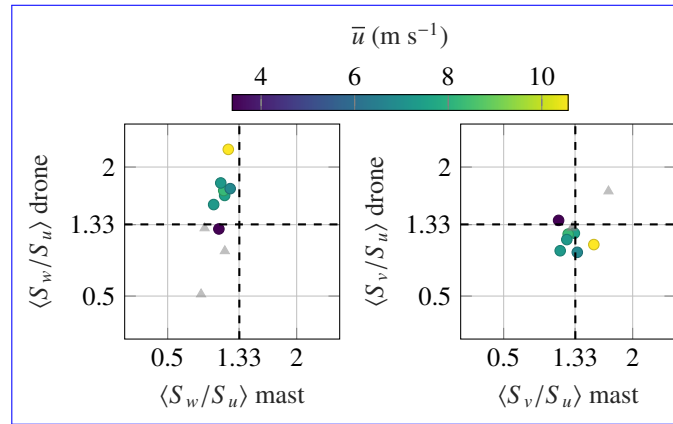
Figure 15. Quadrant analysis for the frequency-averaged spectral ratios $< S_w/S_u >$ (left panel) and $< S_v/S_u >$ (right panel) with $fr > 2$ and $fr < 10$ between the mast and drone-based measurements for different mean wind speeds. The notation $< >$ denotes an average over frequency bins. ~~Only samples~~ Samples with a mean wind speed ~~above $2\,\mathrm{m\,s}^{-1}$~~ below $1\,\mathrm{m\,s}^{-1}$ are ~~included~~ marked as grey triangles, as they are representative of intermittent turbulence, for which the assumption of local isotropy in the inertial subrange may not be defined.

490   their non-stationary nature, which does not fit within the analysis framework. The following discussion and comments exclude these three samples unless explicitly stated otherwise.

Figure 15 shows that ~~at lower wind speeds, SAMURAI-S may provide accurate estimations of the vertical velocity components as $< S_w/S_u >$ is fairly close to~~ only one sample from the drone-based dataset is close to the theoretical ratio of 1.33 for ~~$\overline{u} < 6\,\mathrm{m\,s}^{-1}$. As an opposite trend, SAMURAI-S overestimates this ratio as~~ $< S_w/S_u >$. As wind speed increases, the ratio
495   measured by SAMURAI-S diverges further from 1.33, whereas the mast data ~~display ratios~~ fluctuates between 1.0 and 1.25. ~~While these mast data may be~~ This could be related to the bigger σ_w values measured by the drone setup.

Although the mast data appear closer to the expected ratio of 1.33 compared to the SAMURAI-S, they could still represent an underestimation of up to 20% of the vertical fluctuating component. As discussed above, not achieving the 4/3 ratio may hint at the presence of flow distortion caused by the mast or the sonic anemometer itself, contributing to this underestimation.
500   Similar observations apply for the ratios $< S_v/S_u >$. For $\overline{u} > 6\,\mathrm{m\,s}^{-1}$, the ratio $< S_w/S_u >$ exceeds the expected value of 1.33 in drone measurements.

The ~~recorded data~~ data recorded in this study mainly represent stable or near-neutral atmospheric conditions~~, as ζ was positive for most flights~~. An exception is found in s_1, collected under unstable atmospheric conditions ($\zeta = -0.46$) and ~~features the closest agreement~~ shows one of the closest agreements between the drone and mast-mounted sensors. It should also be noted
505   that for all flights except s_1, the wind consistently came from the 280° to 310° sector. The limited number of samples and the variability in stability and wind direction prevent determining whether the improved agreement under unstable conditions is a systematic effect or influenced by differences in wind direction over heterogeneous topography. Further research is necessary to determine whether convective conditions consistently enhance the performance of the drone-based setup described in this

paper~~or if these observations can be generalized across different turbulence intensities and atmospheric conditions. In addition,~~
~~it is necessary to point out that except for s_1,.~~

5.3 Uncertainties analysis

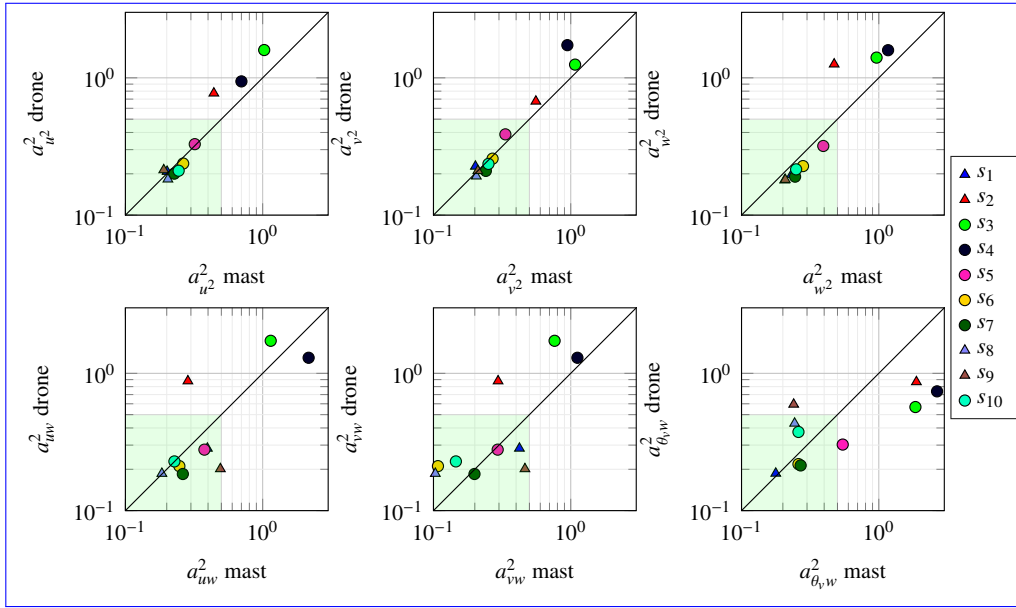Figure 16 presents the uncertainty metrics associated with the calculation of σ_u^2, σ_v^2, σ_w^2, $\overline{u'w'}$, $\overline{v'w'}$, and $\overline{\theta_v'w'}$. Most samples exhibit reasonably low uncertainties, as indicated by the green patch in Fig. 16, which corresponds to a normalised value of 0.5, consistent with that used in Stiperski and Rotach (2016); Cheynet et al. (2019). However, samples s_2, s_3, and s_4 systematically fall outside this green area due to the low wind speed at the time of recording. Consequently, they should not be included in the analysis of turbulence statistics, at least within the framework of stationary homogeneous turbulence. These samples exhibit characteristics of intermittent turbulence, the study of which is beyond the scope of this work.

In Fig. 16, the uncertainty metric $a_{\theta_v w}^2$ shows higher-than-expected uncertainties for samples s_5 and s_9. The relatively high uncertainty for sample s_5 is partly attributable to the short duration of the record—less than $10\,\mathrm{min}$, which results in large uncertainties for covariance estimates. Sample s_9 has a record duration of approximately $17\,\mathrm{min}$, so the high uncertainty value remains unclear, notably since it is only visible in the covariance between the sonic temperature and the vertical velocity component of the ~~wind originates from a sector of 280° to 310° for all other flights. The limited number of samples and the range of stability and wind directions prevent drawing broader conclusions concerning systematic effects~~drone-mounted anemometer. It should be noted that the uncertainty metrics are generally comparable between the drone-based and mast-based measurements, supporting the potential of this mobile platform for turbulence analysis.

6 Conclusions

This study presents a pioneering effort in atmospheric research, focusing on using a research-grade 3D sonic anemometer mounted $18\,\mathrm{m}$ under a drone to observe turbulence. The goal was to assess the effectiveness of drone-mounted sonic anemometers as a versatile tool for turbulence measurement, challenging traditional methods that mount the same sensor on masts or towers. A notable aspect of this research was the application of a dynamic motion compensation algorithm that accounts for the motion and tilt of the sonic anemometer~~while~~. At the same time, the drone hovered above the location of interest. ~~This study also employed the double-rotation method for static tilt correction.~~

Data collection took place during the Models and Observations for Surface Atmosphere Interactions (MOSAI) campaign in France. The methodology included a comparative analysis between conventional mast-mounted 3D sonic anemometers at $30\,\mathrm{m}$ and $60\,\mathrm{m}$ above ground and the drone-mounted anemometer. This comparison focused on mean flow and turbulence ~~characteristics, cross-covariance~~statistics, including the integral length scales, covariance, and auto- and cross-spectral densities of velocity fluctuations. Our findings indicate that the drone-mounted anemometer effectively captures detailed turbulence measurements. Although there is good agreement regarding the along-wind and cross-wind flow when comparing the drone and mast data, ~~the~~drone-based observations consistently overestimate ~~the fluctuations of the vertical wind~~vertical wind fluctuations across all flights~~performed~~. This overestimation increases as the wind speed increases, calling for further analysis under a

Figure 16. Uncertainty metrics (Eqs. (10) to (13)) estimated for the drone-mounted sensor (y-axis) and the mast-mounted sensor (x-axis). The green patch represents the region with low statistical uncertainties.

broader range of wind conditions. Also, our findings show that the drone-mounted sensor and mast-mounted sonic anemometers provide turbulence statistics with similar levels of uncertainty.

For the drone-mounted anemometer, the spectral ratio S_w/S_u was up to 63% larger than the local isotropy hypothesis predicted in the inertial subrange. However, it was also observed that the mast-mounted anemometer could significantly underestimate the vertical turbulence component, with a spectral ratio S_w/S_u that was up to 22% lower than predicted by the local isotropy hypothesis in the inertial subrange.

The sonic temperature and the Obukhov length estimated by both sensors were also investigated. The comparison provides a positive and encouraging overall picture, with good agreement between the mast and drone measurements. The only exception is the shortest sample ($10\,\mathrm{min}$ compared to at least $15\,\mathrm{min}$ for all others), which exhibits markedly divergent behaviour compared to its mast-measured counterpart.

Overall, the findings underscore the ~~reliability of the drone-mounted anemometer in recording the along-wind velocity component and its potential~~ potential of the SAMURAI-S system, especially its complementarity with mast-mounted sonic anemometers and Scanning Doppler wind lidar for ~~the study of atmospheric~~ studying three-dimensional turbulence in the atmosphere.

Appendix A: Trasformation Matrix

The transformation matrix $R(\phi,\theta,\psi)$ is defined as

$$R(\phi,\theta,\psi) = [R_3(\phi)R_2(\theta)R_1(\psi)]^T$$

where

$$R_1(\psi) = \begin{pmatrix} \cos\psi & \sin\psi & 0 \\ -\sin\psi & \cos\psi & 0 \\ 0 & 0 & 1 \end{pmatrix},$$

$$R_2(\theta) = \begin{pmatrix} \cos\theta & 0 & -\sin\theta \\ 0 & 1 & 0 \\ \sin\theta & 0 & \cos\theta \end{pmatrix},$$

$$R_3(\phi) = \begin{pmatrix} 1 & 0 & 0 \\ 0 & \cos\phi & \sin\phi \\ 0 & -\sin\phi & \cos\phi \end{pmatrix}.$$

Appendix B: Power spectral density estimates for other samples

Figure B1 presents the power spectral densities of the three velocity components, as well as the cross-spectral densities between u and w, for samples s_5, s_6, s_8, s_9, and s_{10}, where the concept of spectral density is well-defined. For clarity, these spectral densities are normalised by the variance or covariance of the corresponding variable. Similarly, Fig. B2 displays the normalised power spectral densities of the sonic temperature, along with the normalised co-spectral densities. These figures exhibit trends similar to those observed for samples s_1 and s_7, which were analysed in detail in this study.
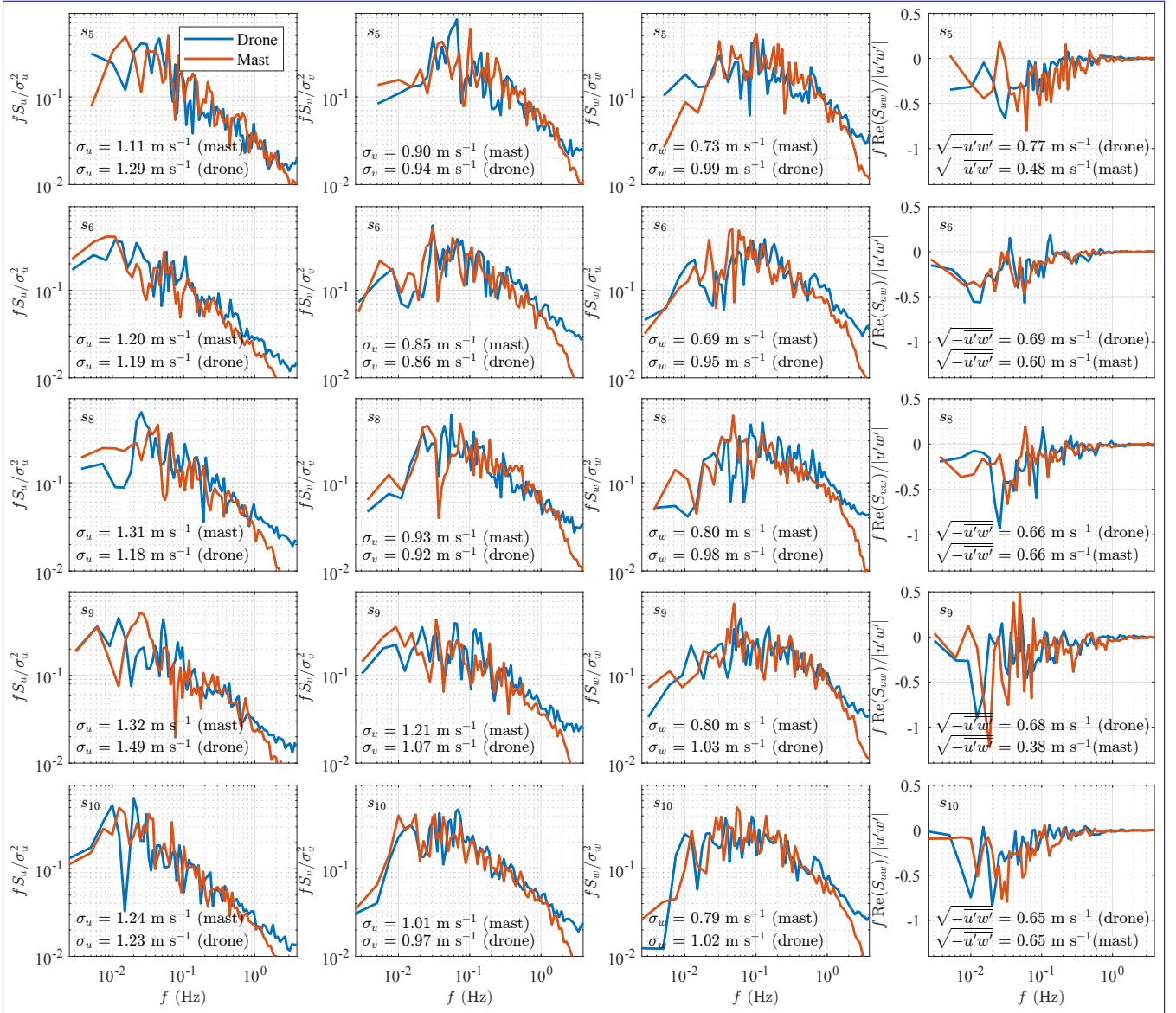
Figure B1. Normalised power spectral densities of the three velocity components and co-spectral densities for samples s_5, s_6, s_8, s_9, and s_{10}.

Figure B2. Normalised power spectral densities of the sonic temperature and associated co-spectral densities for samples s_5, s_6, s_8, s_9, and s_{10}.

References

585 Abichandani, P., Lobo, D., Ford, G., Bucci, D., and Kam, M.: Wind Measurement and Simulation Techniques in Multi-Rotor Small Unmanned Aerial Vehicles, IEEE Access, 8, 54 910–54 927, https://doi.org/10.1109/ACCESS.2020.2977693, 2020.

Alaoui-Sosse, S., Durand, P., Medina, P., Pastor, P., Lothon, M., and Cernov, I.: OVLI-TA: An Unmanned Aerial System for Measuring Profiles and Turbulence in the Atmospheric Boundary Layer, Sensors, 19, 581, http://www.mdpi.com/1424-8220/19/3/581, 2019.

Båserud, L., Reuder, J., Jonassen, M. O., Kral, S. T., Paskyabi, M. B., and Lothon, M.: Proof of concept for turbulence measurements with
590 the RPAS SUMO during the BLLAST campaign, Atmospheric Measurement Techniques, 9, 4901–4913, https://www.atmos-meas-tech.net/9/4901/2016/, 2016.

Beard, R. W. and McLain, T. W.: Small Unmanned Aircraft: Theory and Practice, Princeton University Press, Princeton, United States, 2012.

Busch, N. E. and Panofsky, H. A.: Recent spectra of atmospheric turbulence, Quarterly Journal of the Royal Meteorological Society, 94, 132–148, 1968.

595 Calmer, R., Roberts, G. C., Preissler, J., Sanchez, K. J., Derrien, S., O, and apos;Dowd, C.: Vertical wind velocity measurements using a five-hole probe with remotely piloted aircraft to study aerosol–cloud interactions, Atmospheric Measurement Techniques, 11, 2583–2599, https://www.atmos-meas-tech.net/11/2583/2018/, 2018.

Canut, G., Couvreux, F., Lothon, M., Legain, D., Piguet, B., Lampert, A., Maurel, W., and Moulin, E.: Turbulence fluxes and variances measured with a sonic anemometer mounted on a tethered balloon, Atmospheric Measurement Techniques, 9, 4375–4386,
600 https://doi.org/10.5194/amt-9-4375-2016, 2016.

Chamecki, M. and Dias, N.: The local isotropy hypothesis and the turbulent kinetic energy dissipation rate in the atmospheric surface layer, Quarterly Journal of the Royal Meteorological Society: A journal of the atmospheric sciences, applied meteorology and physical oceanography, 130, 2733–2752, 2004.

Chenglong, L., Zhou, F., Jiafang, W., and Xiang, Z.: A vortex-ring-state-avoiding descending control strategy for multi-rotor UAVs, in: 2015
605 34th Chinese Control Conference (CCC), pp. 4465–4471, https://doi.org/10.1109/ChiCC.2015.7260330, 2015.

Cheynet, E., Jakobsen, J., and Reuder, J.: Velocity Spectra and Coherence Estimates in the Marine Atmospheric Boundary Layer, Boundary-Layer Meteorology, 169, https://doi.org/10.1007/s10546-018-0382-2, 2018.

Cheynet, E., Jakobsen, J. B., and Snæbjörnsson, J.: Flow distortion recorded by sonic anemometers on a long-span bridge: Towards a better modelling of the dynamic wind load in full-scale, Journal of Sound and Vibration, 450, https://doi.org/10.1016/j.jsv.2019.03.013, 2019.

610 Fernando, H. and Weil, J.: Whither the stable boundary layer? A shift in the research agenda, Bulletin of the American Meteorological Society, 91, 1475–1484, 2010.

Flem, A. A., Ghirardelli, M., Kral, S. T., Cheynet, E., Kristensen, T. O., and Reuder, J.: Experimental Characterization of Propeller-Induced Flow (PIF) below a Multi-Rotor UAV, Atmosphere, 15, https://doi.org/10.3390/atmos15030242, 2024.

Foken, T.: 50 years of the Monin-Obukhov similarity theory, Boundary-Layer Meteorology, 119, 431–447, https://doi.org/10.1007/s10546-
615 006-9048-6, 2006.

Foken, T., Aubinet, M., and Leuning, R.: The Eddy Covariance Method, pp. 1–19, Springer Netherlands, Dordrecht, ISBN 978-94-007-2351-1, https://doi.org/10.1007/978-94-007-2351-1_1, 2012.

Forrer, J. and Rotach, M. W.: On the turbulence structure in the stable boundary layer over the Greenland ice sheet, Boundary-Layer Meteorology, 85, 111–136, https://doi.org/10.1023/A:1000466827210, 1997.

620 Ghirardelli, M., Kral, S. T., Müller, N. C., Hann, R., Cheynet, E., and Reuder, J.: Flow Structure around a Multicopter Drone: A Computational Fluid Dynamics Analysis for Sensor Placement Considerations, Drones, 7, 467, https://doi.org/10.3390/drones7070467, 2023.

González-Rocha, J., De Wekker, S. F. J., Ross, S. D., and Woolsey, C. A.: Wind Profiling in the Lower Atmosphere from Wind-Induced Perturbations to Multirotor UAS, Sensors, 20, https://doi.org/10.3390/s20051341, 2020.

Guillermo, P. H., Daniel, A. V., and Eduardo, G. E.: CFD Analysis of two and four blades for multirotor Unmanned Aerial Vehicle, in: 2018
625 IEEE 2nd Colombian Conference on Robotics and Automation (CCRA). IEEE, pp. 1–6, 2018.

Hobby, M. J.: Turbulence Measurements from a Tethered Balloon, Ph.D. thesis, University of Leeds, 2013.

Hofsäß, M., Bergmann, D., Denzel, J., and Cheng, P. W.: Flying UltraSonic–A new way to measure the wind, Wind Energy Science Discussions, pp. 1–21, 2019.

Jin, L., Ghirardelli, M., Mann, J., Sjöholm, M., Kral, S. T., and Reuder, J.: Rotary-wing drone-induced flow – comparison of simulations
630 with lidar measurements, Atmospheric Measurement Techniques, 17, 2721–2737, https://doi.org/10.5194/amt-17-2721-2024, 2024.

Kaimal, J. C. and Finnigan, J. J.: Atmospheric Boundary Layer Flows: Their Structure and Measurement, Oxford university press, 1994.

Kaimal, J. C., Wyngaard, J., Izumi, Y., and Coté, O.: Spectral Characteristics of Surface-Layer Turbulence, Quarterly Journal of the Royal Meteorological Society, 98, 563–589, 1972.

Lei, Y. and Cheng, M.: Aerodynamic performance of a Hex-rotor unmanned aerial vehicle with different rotor spacing, Measurement and
635 Control, 53, 711–718, 2020.

Lei, Y., Ye, Y., and Chen, Z.: Horizontal wind effect on the aerodynamic performance of coaxial Tri-Rotor MAV, Applied Sciences, 10, 8612, 2020.

Li, Z., Pu, O., Pan, Y., Huang, B., Zhao, Z., and Wu, H.: A Study on Measuring the Wind Field in the Air Using a multi-rotor UAV Mounted with an Anemometer, Boundary-Layer Meteorology, 188, 1–27, 2023.

640 Lothon, M., Lohou, F., Pino, D., Couvreux, F., Pardyjak, E. R., Reuder, J., Vilà-Guerau de Arellano, J., Durand, P., Hartogensis, O., Legain, D., Augustin, P., Gioli, B., Lenschow, D. H., Faloona, I., Yagüe, C., Alexander, D. C., Angevine, W. M., Bargain, E., Barrié, J., Bazile, E., Bezombes, Y., Blay-Carreras, E., van de Boer, A., Boichard, J. L., Bourdon, A., Butet, A., Campistron, B., de Coster, O., Cuxart, J., Dabas, A., Darbieu, C., Deboudt, K., Delbarre, H., Derrien, S., Flament, P., Fourmentin, M., Garai, A., Gibert, F., Graf, A., Groebner, J., Guichard, F., Jiménez, M. A., Jonassen, M., van den Kroonenberg, A., Magliulo, V., Martin, S., Martinez, D., Mastrorillo, L., Moene, A. F., Molinos,
645 F., Moulin, E., Pietersen, H. P., Piguet, B., Pique, E., Román-Cascón, C., Rufin-Soler, C., Saïd, F., Sastre-Marugán, M., Seity, Y., Steeneveld, G. J., Toscano, P., Traullé, O., Tzanos, D., Wacker, S., Wildmann, N., and Zaldei, A.: The BLLAST field experiment: Boundary-Layer Late Afternoon and Sunset Turbulence, Atmospheric Chemistry and Physics, 14, 10 931–10 960, https://doi.org/10.5194/acp-14-10931-2014, 2014.

Mahrt, L.: Stably stratified atmospheric boundary layers, Annual Review of Fluid Mechanics, 46, 23–45, 2014.

650 Mansour, M., Kocer, G., Lenherr, C., Chokani, N., and Abhari, R. S.: Seven-Sensor Fast-Response Probe for Full-Scale Wind Turbine Flowfield Measurements, Journal of Engineering for Gas Turbines and Power, 133, 081 601, http://gasturbinespower.asmedigitalcollection. asme.org/article.aspx?articleid=1428610, 2011.

Marcq, S. and Weiss, J.: Influence of sea ice lead-width distribution on turbulent heat transfer between the ocean and the atmosphere, The Cryosphere, 6, 143–156, 2012.

655 Mauder, M., Cuntz, M., Drüe, C., Graf, A., Rebmann, C., Schmid, H. P., Schmidt, M., and Steinbrecher, R.: A strategy for quality and uncertainty assessment of long-term eddy-covariance measurements, Agricultural and Forest Meteorology, 169, 122–135, https://doi.org/10.1016/j.agrformet.2012.09.006, 2013.

Mauder, M., Foken, T., Aubinet, M., and Ibrom, A.: Eddy-covariance measurements, in: Springer Handbook of Atmospheric Measurements, pp. 1473–1504, Springer, 2021.

660 McMillen, R. T.: An eddy correlation technique with extended applicability to non-simple terrain, Boundary-Layer Meteorology, 43, 231–245, https://doi.org/10.1007/BF00128405, 1988.

Midjiyawa, Z., Cheynet, E., Reuder, J., Ágústsson, H., and Kvamsdal, T.: Potential and challenges of wind measurements using met-masts in complex topography for bridge design: Part II – Spectral flow characteristics, Journal of Wind Engineering and Industrial Aerodynamics, 211, 104 585, https://doi.org/10.1016/j.jweia.2021.104585, 2021.

665 Monin, A. S. and Obukhov, A. M.: Basic laws of turbulent mixing in the surface layer of the atmosphere, Contrib. Geophys. Inst. Acad. Sci. USSR, 151, e187, 1954.

Natalie, V. A. and Jacob, J. D.: Experimental Observations of the Boundary Layer in Varying Topography with Unmanned Aircraft, in: AIAA Aviation 2019 Forum, American Institute of Aeronautics and Astronautics, https://doi.org/10.2514/6.2019-3404, 2019.

Ogawa, Y. and Ohara, T.: Observation of the turbulent structure in the planetary boundary layer with a kytoon-mounted ultrasonic anemometer
670 system, Boundary-Layer Meteorology, 22, 123–131, https://doi.org/10.1007/BF00128060, 1982.

Olesen, H. R., Larsen, S. E., and Højstrup, J.: Modelling velocity spectra in the lower part of the planetary boundary layer, Boundary-Layer Meteorology, 29, 285–312, 1984.

Palomaki, R. T., Rose, N. T., van den Bossche, M., Sherman, T. J., and Wekker, S. F. D.: Wind estimation in the lower atmosphere using multirotor aircraft, Journal of Atmospheric and Oceanic Technology, 34, 1183–1191, 2017.

675 Peña, A., Dellwik, E., and Mann, J.: A method to assess the accuracy of sonic anemometer measurements, Atmospheric Measurement Techniques, 12, 237–252, 2019.

Porté-Agel, F., Bastankhah, M., and Shamsoddin, S.: Wind-turbine and wind-farm flows: A review, Boundary-Layer Meteorology, 174, 1–59, 2020.

Prudden, S., Fisher, A., Mohamed, A., and Watkins, S.: A flying anemometer quadrotor: Part 1, 7th International Micro Air Vehicle Confer-
680 ence and Competition - Past, Present and Future, 2016.

Rautenberg, A., Schön, M., zum Berge, K., Mauz, M., Manz, P., Platis, A., van Kesteren, B., Suomi, I., Kral, S. T., and Bange, J.: The Multi-Purpose Airborne Sensor Carrier MASC-3 for Wind and Turbulence Measurements in the Atmospheric Boundary Layer, Sensors, 19, 2292, https://doi.org/10.3390/s19102292, 2019.

Segales, A. R., Greene, B. R., Bell, T. M., Doyle, W., Martin, J. J., Pillar-Little, E. A., and Chilson, P. B.: The CopterSonde: an insight into
685 the development of a smart unmanned aircraft system for atmospheric boundary layer research, Atmospheric Measurement Techniques, 13, 2833–2848, https://doi.org/10.5194/amt-13-2833-2020, 2020.

Shelekhov, A., Afanasiev, A., Shelekhova, E., Kobzev, A., Tel'minov, A., Molchunov, A., and Poplevina, O.: Using small unmanned aerial vehicles for turbulence measurements in the atmosphere, Izvestiya, Atmospheric and Oceanic Physics, 57, 533–545, 2021.

Shimura, T., Inoue, M., Tsujimoto, H., Sasaki, K., and Iguchi, M.: Estimation of Wind Vector Profile Using a Hexarotor Unmanned Aerial
690 Vehicle and Its Application to Meteorological Observation up to 1000 m above Surface, Journal of Atmospheric and Oceanic Technology, 35, 1621 – 1631, https://doi.org/10.1175/JTECH-D-17-0186.1, 2018.

Stiperski, I. and Rotach, M. W.: On the Measurement of Turbulence Over Complex Mountainous Terrain, Boundary-Layer Meteorology, 159, 97–121, https://doi.org/10.1007/s10546-015-0103-z, 2016.

Talaeizadeh, A., Antunes, D., Pishkenari, H. N., and Alasty, A.: Optimal-time quadcopter descent trajectories avoiding the vortex ring and
695 autorotation states, Mechatronics, 68, 102 362, https://doi.org/https://doi.org/10.1016/j.mechatronics.2020.102362, 2020.

Taylor, P. C., Hegyi, B. M., Boeke, R. C., and Boisvert, L. N.: On the Increasing Importance of Air-Sea Exchanges in a Thawing Arctic: A Review, Atmosphere, 9, https://doi.org/10.3390/atmos9020041, 2018.

Thielicke, W., Hübert, W., Müller, U., Eggert, M., and Wilhelm, P.: Towards accurate and practical drone-based wind measurements with an ultrasonic anemometer, Atmospheric Measurement Techniques, 14, 1303–1318, 2021.

700   Tieleman, H. W.: Universality of velocity spectra, Journal of Wind Engineering and Industrial Aerodynamics, 56, 55–69, 1995.

Van der Hoven, I.: Power spectrum of horizontal wind speed in the frequency range from 0.0007 to 900 cycles per hour, Journal of Meteorology, 14, 160–164, 1957.

Veers, P., Dykes, K., Lantz, E., Barth, S., Bottasso, C. L., Carlson, O., Clifton, A., Green, J., Green, P., Holttinen, H., et al.: Grand challenges in the science of wind energy, Science, 366, eaau2027, 2019.

705   Welch, P.: The use of fast Fourier transform for the estimation of power spectra: a method based on time averaging over short, modified periodograms, IEEE Transactions on Audio and Electroacoustics, 15, 70–73, 1967.

Wetz, T., Wildmann, N., and Beyrich, F.: Distributed wind measurements with multiple quadrotor unmanned aerial vehicles in the atmospheric boundary layer, Atmospheric Measurement Techniques, 14, 3795–3814, 2021.

Wildmann, N. and Wetz, T.: Towards vertical wind and turbulent flux estimation with multicopter uncrewed aircraft systems, Atmospheric
710   Measurement Techniques, 15, 5465–5477, 2022.

Wildmann, N., Hofsäß, M., Weimer, F., Joos, A., and Bange, J.: MASC – a small Remotely Piloted Aircraft (RPA) for wind energy research, Advances in Science and Research, 11, 55–61, http://www.adv-sci-res.net/11/55/2014/, 2014a.

Wildmann, N., Ravi, S., and Bange, J.: Towards higher accuracy and better frequency response with standard multi-hole probes in turbulence measurement with remotely piloted aircraft (RPA), Atmospheric Measurement Techniques, 7, 1027–1041, http://www.atmos-meas-tech.
715   net/7/1027/2014/, 2014b.

Wilson, T. C., Brenner, J., Morrison, Z., Jacob, J. D., and Elbing, B. R.: Wind Speed Statistics from a Small UAS and Its Sensitivity to Sensor Location, Atmosphere, 13, https://www.mdpi.com/2073-4433/13/3/443, 2022.

Witte, B., Singler, R., and Bailey, S.: Development of an Unmanned Aerial Vehicle for the Measurement of Turbulence in the Atmospheric Boundary Layer, Atmosphere, 8, 195, http://www.mdpi.com/2073-4433/8/10/195, 2017.

720   Wu, L. and Qiao, F.: Wind Profile in the Wave Boundary Layer and Its Application in a Coupled Atmosphere-Wave Model, Journal of Geophysical Research: Oceans, 127, 1–15, https://doi.org/10.1029/2021JC018123, 2022.

Wyngaard, J. C.: On Surface Layer Turbulence, in: Workshop on Micrometeorology, edited by Haugen, D. A., pp. 101–150, American Meteorological Society, Boston, 1973.